Remote Sensing of Environment 318 (2025) 114596

Contents lists available at ScienceDirect

Remote Sensing of Environment

journal homepage: www.elsevier.com/locate/rse

A multi-layer perceptron approach for SIF retrieval in the O_2-A absorption band from hyperspectral imagery of the HyPlant airborne sensor system

Jim Buffat [a,d,*], Miguel Pato [b], Kevin Alonso [c], Stefan Auer [b], Emiliano Carmona [b], Stefan Maier [b], Rupert Müller [b], Patrick Rademske [a], Bastian Siegmann [a], Uwe Rascher [a], Hanno Scharr [d]

[a] Forschungszentrum Jülich GmbH, Institute of Bio- and Geosciences, IBG-2: Plant Sciences, Jülich, Germany
[b] Remote Sensing Technology Institute, German Aerospace Center (DLR), Oberpfaffenhofen, Germany
[c] Starion Group c/o European Space Agency (ESA), Largo Galileo Galilei, Frascati 00044, Italy
[d] Forschungszentrum Jülich GmbH, Institute of Advanced Simulations, IAS-8: Data Analytics and Machine Learning, Jülich, Germany

ARTICLE INFO

Keywords:
Solar-induced fluorescence
Spectral fitting methods
Deep learning
Neural networks
Hyperspectral sensors
Remote sensing
SIF retrieval

ABSTRACT

Accurate estimation of solar-induced fluorescence (SIF) from passively sensed hyperspectral remote sensing data has been identified as fundamental in assessing the photosynthetic activity of plants for various scientific and ecological applications at different spatial scales. Different techniques to derive SIF have been developed over the last decades. In view of ESA's upcoming Earth Explorer satellite mission FLEX aiming to provide high-quality global imagery for SIF retrieval an increased interest is placed in physical approaches. We present a novel method to retrieve SIF in the O_2-A absorption band of hyperspectral imagery acquired by the HyPlant sensor system. It aims at a tight integration of physical radiative transfer principles and self-supervised neural network training. To this end, a set of spatial and spectral constraints and a specific loss formulation are adopted. In a validation study we find good agreement between our approach and established retrieval methods as well as with in-situ top-of-canopy SIF measurements. In two application studies, we additionally find evidence that the estimated SIF (i) satisfies a first-order model of diurnal SIF variation and (ii) locally adapts the estimated optical depth in topographically variable terrain.

1. Introduction

The notion that sun-induced fluorescence (SIF) is an important biophysical parameter has become prevalent over the last decades (Mohammed et al., 2019). In the last two decades, sensor and retrieval method development, on the one hand, and the push for the standardization of hyperspectral imagery in airborne and spaceborne sensing systems, on the other hand, have set the path to establish spatially contiguous SIF estimates (Grace et al., 2007; Rascher et al., 2009; Guanter et al., 2013; Ryu et al., 2019). The close causal link of the SIF signal to the internal photosynthetic machinery of plants is a valuable tool to infer plant dynamics remotely over large areas. SIF has found applications linked to establishing regional and global gross primary productivity and light-use efficiency of vegetation (Joiner et al., 2013; Cheng et al., 2013; Sun et al., 2018), small and large scale quantification of photosynthetic dynamics (Porcar-Castell et al., 2014; Rossini et al., 2015), the detection of various vegetation stress types (van der Tol et al., 2014; Verrelst et al., 2015; Damm et al., 2022), vegetative transpiration rates (Maes et al., 2020), and ecological monitoring more generally (Damm et al., 2015, 2020; Colombo et al., 2018). The retrieval of SIF from airborne hyperspectral imagery in particular allows to follow spatial and temporal patterns of photosynthetic activity at meter to submeter resolution. This provides important information for precision farming and phenotyping applications and was investigated in the context of food production (Bendig et al., 2021).

A range of hyperspectral sensors on different platforms exist for operational passive retrieval of top-of-canopy SIF (Bandopadhyay et al., 2020). In the proximal SIF retrieval, the use of field spectrometers has grown in recent years due to increased interest in passive SIF measurements as indicators of plant status in application studies. Furthermore, these ground measurements are important in the development of UAV-based, airborne and spaceborne sensors for SIF retrieval. High-quality hyperspectral ground data sets for calibration and validation of non-ground-based sensors are increasingly needed (Naethe et al., 2024) as the number of SIF products increases. In recent years, a multitude of globally distributed spaceborne SIF products have been developed from sensors that were originally designed for the characterization of the atmosphere such as GOSAT (Joiner et al., 2011), GOME (Joiner et al., 2013; Guanter et al., 2014), SCIAMACHY (Joiner et al., 2016),

* Corresponding author at: Forschungszentrum Jülich GmbH, Institute of Bio- and Geosciences, IBG-2: Plant Sciences, Jülich, Germany.
E-mail address: j.buffat@fz-juelich.de (J. Buffat).

https://doi.org/10.1016/j.rse.2024.114596
Received 13 April 2024; Received in revised form 23 November 2024; Accepted 30 December 2024
Available online 15 January 2025

OCO-2 (Sun et al., 2017), TROPOMI (Guanter et al., 2015a, 2021) and TanSAT (Yao et al., 2021). In addition, the upcoming FLEX satellite mission will make available data from the first hyperspectral sensor dedicated full-spectrum SIF retrieval on a global scale by 2026 (Drusch et al., 2017).

Investigations regarding the development, improvement and testing of operational SIF retrieval algorithms have relied strongly on data from airborne platforms equipped with sensors such as with the micro-hyperspectral imaging sensor (Zarco-Tejada et al., 2016), with the Chlorophyll Fluorescence Imaging Spectrometer (CFIS) (Frankenberg et al., 2018) and with the HyPlant spectrometer (Siegmann et al., 2019). The development of the new SIF retrieval approach presented in this work is based on hyperspectral HyPlant imagery. HyPlant data is particularly suitable to testing new retrieval methods as it has been designed as an airborne demonstrator for the FLORIS sensor of the upcoming spaceborne FLEX mission. Moreover, hundreds of HyPlant flight lines were recorded in several field campaigns since 2014. This large collection of hyperspectral data sets allowed to test different SIF retrieval methods (European Space Agency, 2017a,b, 2018, 2019; Rascher et al., 2021, 2022a,b). Many of these data sets are acquired in tandem with ground-based measurements allowing to derive high quality ground-based SIF estimates as 'ground truth' in addition to the hyperspectral flight lines (see Section 2.2 for details on the data sets and ground measurements).

Prominent algorithms for SIF retrieval on hyperspectral data are the 3FLD method (Maier et al., 2004), the Improved Fraunhofer Line Discrimination (iFLD) (Alonso et al., 2008), the Spectral Fitting Method (SFM) targeting SIF in oxygen absorption bands (Mazzoni et al., 2012; Meroni et al., 2010) as well as full-spectrum SFM (Cogliati et al., 2015b, 2018, 2019) developed in view of the ambitious accuracy requirements of the FLEX mission, the Singular Vector Decomposition (SVD) method (Guanter et al., 2012) as well as the recently developed partial least-squares (PLS) approach (Naethe et al., 2022). In this work, we examine the performance of a new spectral fitting method neural network (called SFMNN) with a novel self-supervised loss function specifically formulated for SIF retrieval from hyperspectral imagery first presented in Buffat et al. (2023) and compare it to SFM (Cogliati et al., 2015b) and iFLD (Wieneke et al., 2016) versions adapted to SIF retrieval in the O_2-A absorption band of HyPlant acquisitions. The current work restricts the model fitting to the O_2-A band which is a subset of the radiance spectrum measured by HyPlant. While restricting the spectral range decreases the amount of constraining information during training it also decreases the complexity and, thus, the required complexity of the physical model fitted to the data. Fitting the whole HyPlant spectrum with the proposed methodology for full-spectrum SIF retrieval is, however, principally possible. It can be achieved by adjusting the formulation of the physical at-sensor radiance simulation. In this contribution we have, however, opted to present a more concise retrieval problem in the O_2-A band in order to discuss our methodology.

As in other spectral fitting retrieval schemes we aim at performing a decomposition of the at-sensor radiance into reflected irradiance and the top-of-canopy fluorescence transmitted to the optical sensor. We investigate the use of a neural network to learn a feature based decomposition instead of leveraging pixelwise optimization as is implemented in other spectral fitting methods. This decomposition requires a joint estimation of the surface reflectance, the top-of-canopy fluorescence and the influence of atmospheric transmittance and scattering during data acquisition, which cannot be inferred based on physical principles alone due to incomplete knowledge of the atmospheric composition and the surface properties at acquisition time. In its most general form such a joint estimation constitutes an ill-posed inversion problem as different decompositions can result in the same observation (Frankenberg et al., 2011). We introduce constraints based on prior knowledge of the spectral forms and spatial variability of the atmospheric transfer functions, the surface reflectance and the fluorescence emission in the O_2-A absorption band to reduce the space of possible solutions. A similar set-up has been adopted in earlier SFM implementations restricted to the O_2-A and O_2-B absorption band (Mazzoni et al., 2012; Meroni et al., 2010) as well as for full-spectrum retrieval (Cogliati et al., 2015b, 2019).

Fluorescence and reflectance are spectrally smooth, but vary strongly in space depending mainly on the distribution of vegetation, the photosynthetic state of the vegetation and soil conditions. In contrast to this, atmospheric functions are spectrally highly variable but spatially smooth as they vary on spatial scales that are larger than the typical spatial footprints of airborne imagery (Anderson et al., 2003; Thompson et al., 2021) which allows the simplifying assumption of constant atmospheric conditions over extended spatial domains for the purpose of fluorescence estimation. Atmospheric transfer functions are therefore typically estimated for entire flight lines or large spatial image regions in existing SIF retrieval schemes.

To disentangle fluorescence and reflectance, iFLD and SFM formulate pixelwise functional constraints, i.e. constraints on full spectra or on a collection of spectral lines, that either allow to fit a specific at-sensor radiance model (SFM) or else to solve an equation system (iFLD). However, the assumption of constant atmospheric conditions causes performance decreases in regions with variable atmospheric transfer properties, e.g., because of varying optical path lengths due to variable topography, aerosol and water vapor concentrations, temperature and pressure profiles and clouds (Sabater et al., 2021; Guanter et al., 2010; Pato et al., 2024). Disregarding such atmospheric variability can result in misattribution of signal components in the decomposition that SIF retrieval methods perform. Changing optical path lengths results in variable absorption of oxygen and, thus, in changing O_2-A absorption depths. These changes cannot be attributed uniquely to the presence of fluorescence anymore as a result. In cases where the atmospheric transfer functions cannot be assumed sufficiently constant in the spatial dimension, localized estimates of the atmospheric transfer or an atmospheric correction of the at-sensor radiance is necessary. If retrieval methods do not rely on atmospherically corrected data, but characterize the atmosphere on-the-fly (such as the iFLD and SFM baseline methods in this contribution), they must be run repeatedly on independent localized subsets of the data where the assumption of constant topography holds approximately. This results in a computational overhead and exposes the retrieval to errors incurred due to the spatial discretization of the input data. While approaches for computationally efficient estimation of spatially variable atmospheric transfer exists (Thompson et al., 2022), such approaches have not been integrated in existing SIF retrieval methods. The introduction of atmospheric correction on the other hand exposes the SIF retrieval to errors in misparameterization of the correction algorithm, particularly in acquisition contexts where only incomplete knowledge of the atmospheric components exists (van der Tol et al., 2023). For this reason, a practical contribution of this study is that our new retrieval method allows for locally varying atmospheric conditions and, thus, is able to provide SIF estimates for topographically complex terrains. The proposed method does not rely on a separate atmospheric characterization or correction step as in SFM and iFLD since the estimation of the atmospheric transfer functions is learned as part of a joint estimation problem.

Recently published neural network based SIF retrieval schemes focus on reconstructing traditionally derived spaceborne SIF products from reflectance and PAR products and a subset of high-quality SIF estimates used as labels (Gentine and Alemohammad, 2018; Zhang et al., 2018; Chen et al., 2022). Our approach is different to these approaches as we do not use labels for training, but leverage a set of constraints to invert a physical model of the at-sensor radiance. Our approach uses similar model assumptions as SFM (Cogliati et al., 2015b) for the different parts of the at-sensor radiance model, i.e., the fluorescence, reflectance, and atmospheric functions, since the at-sensor radiance needs to be simulated efficiently during the loss minimization of SFMNN. In the case of SFMNN we additionally require

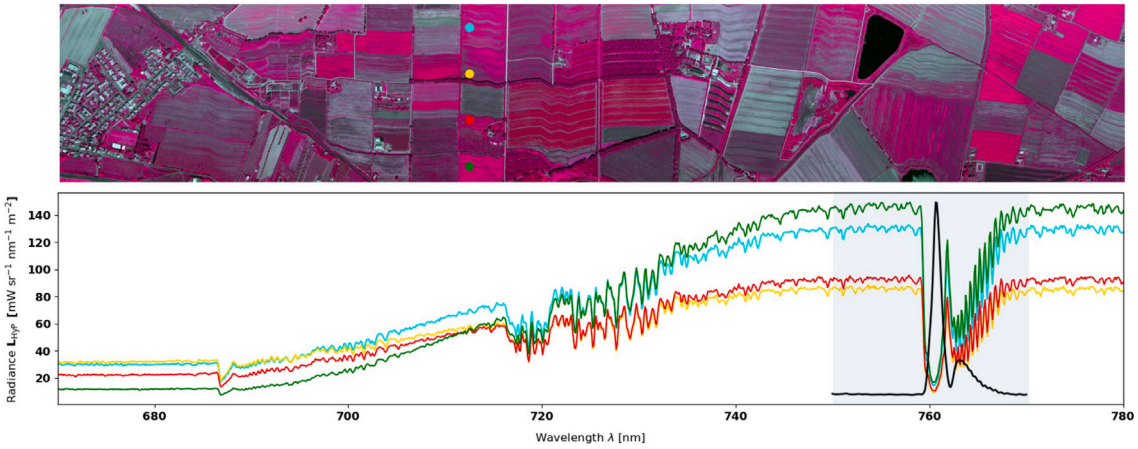

Fig. 1. Sample spectra of a WST-2019 HyPlant acquisition (false color image (FLUO NIR, red and green), upper row) over the input spectral window (lower row) $\mathcal{W}_{\text{tot}}$. The window $\mathcal{W}$ (750–770 nm) simulated by our approach is highlighted in blue. In black we show the SNR based weighting w_f described in Section 3.4.1. (For interpretation of the references to color in this figure legend, the reader is referred to the web version of this article.)

a simulation model from which a gradient can be derived easily with automatic differentiation.

This work encompasses a qualitative comparison of the reconstruction residuals of SFMNN as compared to SFM and a quantitative comparison of its SIF predictions with FLOX top-of-canopy SIF measurements. Additionally, we show in two application studies that SFMNN's SIF predictions are in line with physiological and physical plausibility considerations.

In the first application study, we analyze the diurnal course of SFMNN predicted SIF. Understanding the diurnal dynamics of canopy SIF and its interplay with plant status and photosynthetic activity is an open and relevant research question (Lee et al., 2015; Kim et al., 2021; Siegmann et al., 2021; Pierrat et al., 2022). SIF as a function of daytime has been modeled in the past by van der Tol et al. (2016) and has been the subject of detailed studies more recently (Wang et al., 2021; Chang et al., 2021). As a plausibility check of SFMNN SIF predictions, we can make use of the universal feature of diurnal SIF dynamics to be strongly correlated to the local solar irradiance due to the large dependency of SIF on available photosynthetically active radiation (PAR). Given a predicted SIF time series we can formulate a first order plausibility test on whether the predicted SIF peaks around solar noon.

The SFMNN prediction of the atmospheric transfer is designed to be locally adaptive. The second application study focuses therefore on the sensitivity of the atmospheric transfer prediction to changing atmospheric and observational conditions. Due to a lack of knowledge about the atmospheric state at the time of data acquisition, we cannot compare the predicted atmospheric conditions to a measured or estimated atmospheric composition to gain insights into the physical accuracy of the predicted optical depth of the atmosphere. The only driver of the atmospheric transfer that can be quantitatively assessed by us is the optical path length of a given pixel on the ground. Therefore we test SFMNN's capacity to adapt to local changes in the optical path in HyPlant acquisitions with considerable topographic variation.

2. Data

2.1. HyPlant spectrometer

HyPlant is an assembly of two hyperspectral push-broom sensors with different spectral sampling and resolution configurations. The FLUO module covers the range 670–780 nm with a spectral sampling interval of 0.11 nm. Its resolution in terms of the full width half maximum (FWHM) is 0.27 nm (Siegmann et al., 2019). See Fig. 1 for sample spectra over the full spectral range of HyPlant. The DUAL module in contrast, provides optical data in the spectral range 370–2500 nm with 3–10 nm spectral sampling and a FWHM varying between 1.7–5.6 nm. The FLUO module was specifically designed for SIF retrieval in the O_2-A and O_2-B absorption bands when operated on airborne platforms at flight heights varying from 350 m to 1800 m. The DUAL module's purpose is to simultaneously provide optical data from which ancillary information, such as the reflectance and various related products (e.g., the photochemical reflectance index (PRI) or the Enhanced Vegetation Index (EVI) (Bandopadhyay et al., 2019)), can be derived. The current work makes use of radiometrically calibrated FLUO acquisitions in sensor geometry as input for the SIF predictor network (Buffat et al., 2024b). The input data is not spectrally calibrated. Rather, the spectral calibration is estimated as part of the SIF retrieval scheme presented here .

We train a neural network (see Fig. 2) with data from 13 HyPlant campaigns in five locations from six years listed in Table 1. The measurement campaigns used for training cover a wide range of the nominal flight heights at which HyPlant is operated (350–1800 m). The acquisitions of these campaigns also differ with respect to the variability of the ground altitude. NRS-2019, TR32-2019, GLO-2019, INN-2022 and SOP-2023 comprise acquisitions with ground altitude changes of 50–150 m, while WST-2019, SEL-2018 and the CKA campaigns were conducted over flat terrain (less than 20 m). The diversity of sun-surface-sensor geometries over this multi-year data set results in significant variability of the O_2-A absorption band depth.

The training process of our method involves a pretraining on a large and variable data set and subsequent finetuning to smaller data sets consisting of HyPlant imagery acquired at the same nominal flight height and comparable topographic variation. During pretraining the model is trained to minimize the same loss as during finetuning. Pretraining is conducted to derive a coarse base predictor which then can be finetuned to different datasets. From this base predictor data set specific models can be derived with fewer training steps than a full training process would require. We expect the variability of the fitted atmospheric transfer functions during finetuning to be smaller than in the full data set such that finetuning also aims at improving the base predictors performance for the specific atmospheric transfer conditions prevalent in different data sets.

For the pretraining we compiled a data set D_{mix} consisting of acquisitions with large differences in nominal flight height and topographic conditions (see Table 2). The variability of this data set ensured the generalization capacity of the coarse model to a wide variety of observation conditions during finetuning.

For finetuning, we created the data sets D_{350}, D_{600} and D_{1500} for individual nominal flight height by selecting a subset of the available acquisitions of the measurement campaigns with small topographic

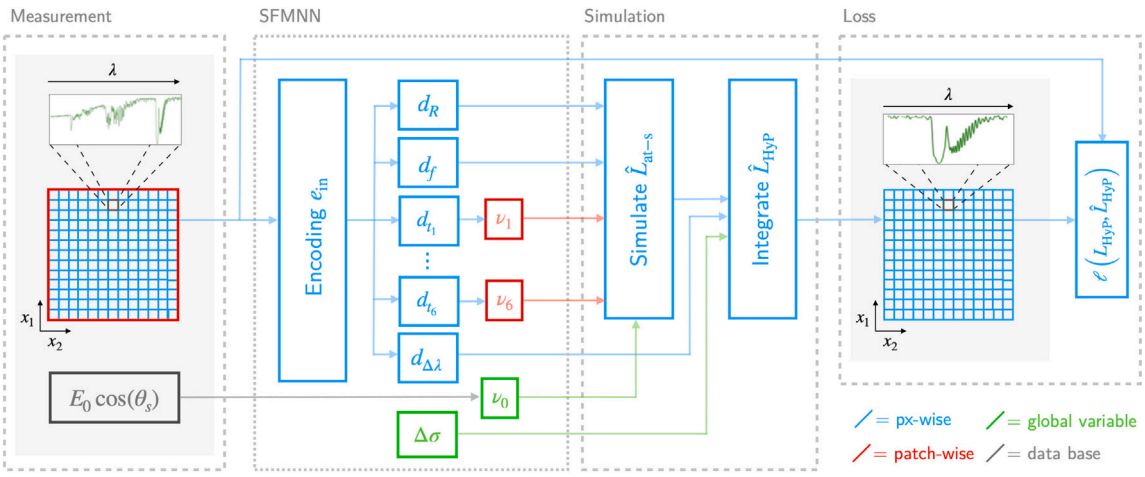

Fig. 2. Outline of SFMNN's data input and architecture. Hyperspectral image patches are encoded (e_{in}) in a pixel-wise fashion to a common latent space. The latent vectors are subsequently decoded to physical variables (d_R, d_f, …) parameterizing a four-stream model simulating the high-resolution at-sensor radiance $\hat{L}_{\text{at-s}}$. The patchwise decodings (d_{t_1}, …, d_{t_6}) are homogenized across the patch for that purpose. In a second simulation step, the estimated sensor characterization ($\Delta\lambda, \Delta\sigma$) is applied to $\hat{L}_{\text{at-s}}$ in order to yield a reconstructed observation $\hat{L}_{\text{HyP}}$. Different colors denote the range over which variables are kept constant (*px-wise* varying in every pixel, *patch-wise* over patches, *global-variable* over a single training data set). *data base* denotes the origin of the solar irradiance model (Kurucz, 2006) and solar zenith angle θ_s calculated for each acquisition. (For interpretation of the references to color in this figure legend, the reader is referred to the web version of this article.)

Table 1
Campaign data sets acquired in different locations in the years 2018–2023. With FLOX we denote the availability of simultaneous FLOX data, with Δh the maximum topographic variation over the campaign data set, with *HyP* the corresponding campaign report and with *DEM* corresponding the digital elevation map used for validation purposes. All campaign data sets and corresponding FLOX measurements are available (Buffat et al., 2024b) .

Campaign data set	FLOX	Δh [m]	HyP	DEM	Location
SEL-2018 (600 m)	✓	20	Rascher et al. (2021)	–	Selhausen, DE
SEL-2019 (600 m)	–	20	Rascher et al. (2022a)	–	
SEL-2022 (600 m)	–	20	–	–	
WST-2019 (1500 m)	✓	20	Rascher et al. (2022a)	–	Braccagni, IT
NRS-2019 (1500 m)	–	70	Rascher et al. (2022a)	Tarquini et al. (2023)	
TR32-2019 (1800 m)	–	150	Rascher et al. (2022a)	Nordrhein-Westfalen (2017)	Jülich, DE
INN-2022 (350 m)	–	60	–	Nordrhein-Westfalen (2017)	
SOP-2023 (600 m)	–	140	–	Nordrhein-Westfalen (2017)	
CKA-2020 (350 m)	✓	20	–	–	Klein
CKA-2020 (600 m)	✓	20	–	–	Altendorf, DE
CKA-2021 (350 m)	✓	20	–	–	
CKA-2022 (350 m)	✓	20	–	–	
GLO-2021 (1150 m)	✓	70	Rascher et al. (2022b)	NASA JPL (2013)	Mollerussa, ES

variation within single acquisitions (see *flat* in Table 2). The number of patches per finetuning data set differs depending on data availability at individual flight heights. We selected acquisitions for individual both the pretraining and finetuning data sets by hand to ensure a balanced distribution of the sun-zenith angles (SZA) at which the acquisitions were recorded.

Parallelly, we created data sets with strong topographic variability (see *topo* in Table 2). As for the *flat* denoted data sets, we grouped together campaign data sets acquired at the same flight height. Differently to $\mathcal{D}_{\text{mix}}$ we group the acquisitions according to the nominal flight height in the *topo* data sets. Due to data limitations, the compiled *topo* data sets are smaller and constrained to single campaign site and acquisition years in all but one case. Since the baseline iFLD and SFM implementations are not adapted to SIF retrieval under variable topography (see Section 2.3), we cannot validate the SFMNN SIF predictions in acquisitions of these datasets directly. Instead, we perform a plausibility study in Section 4.4.

An additional data set $\mathcal{D}_{\text{day}}$ was compiled for validation purposes. It is used both for validating SFMNN's reconstruction performance as well as the physiological plausibility of our approach in the first application study. It consists of nine repeated flights over the same location at the same nominal flight height in an irregular frequency (10:11, 10:19, 10:27, 10:34, 13:15, 13:30, 13:38, 16:11, 16:18 CEST) allowing us to validate the performance of our approach under different solar zenith angles with otherwise comparable conditions. For our analysis of the SFMNN predicted diurnal course of SIF, we leverage the universal property of SIF to be strongly correlated to PAR under non-shaded conditions. This correlation is however only expected to be fulfilled over homogeneous fields. It may be invalid only under strongly changing irradiation in pixels with complex 3D structure. Under such conditions, (i) varying sampling directions of the angular SIF emission distribution and (ii) shade impede the comparability of measurements at different times during the day. Predictions of the $\mathcal{D}_{\text{day}}$ data set are well suited for this analysis as the acquisitions have a relatively large pixel footprint (2.3 m) due to the large nominal flight height (1500 m). At this pixel resolution small scale inhomogeneities in crop fields are not preserved.

2.2. In-situ fluorescence measurements

A subset of the HyPlant measurement campaigns presented in Table 1 were accompanied by in-situ radiance and irradiance measurements recorded by the FLOX system (Fluorescence Box, JB-Hyperspectral Devices GmbH, Düsseldorf, Germany) (Buffat et al., 2024b). The FLOX system provides precise radiance top-of-canopy measurements within

Table 2
Compiled data sets of HyPlant acquisitions from flight campaigns in the years 2018–2023. Flight heights are not mentioned if indicated in the data set name. In the first column, we indicate the purpose of the data set: *flat* or *topo* denote the training of predictors for flat or topographically variable terrain, *val.* denotes specific validation purposes outlined in the Results section, *pretrain* denotes the pretraining of a common predictor. $|D|$ denotes the number of used 17 × 17 patches [$\times 10^3$] and in brackets the number of used acquisitions.

Data set		Included campaign data sets	$\|D\|$
pretrain	D_{mix}	SEL-2018 (600 m), NRS-2019 (1500 m), WST-2019 (1500 m), CKA-2021 (350 m), GLO-2021 (1150 m)	260 (44)
flat	D_{350}	CKA-2020, CKA-2021, CKA-2022	183 (44)
	D_{600}	SEL-2018, SEL-2019, SEL-2020, SEL-2022, CKA-2019, CKA-2020	283 (32)
	D_{1500}	WST-2019	54 (16)
topo	D^t_{600}	INN-2022, SOP-2023	107 (12)
	D^t_{1150}	GLO-2021	100 (8)
	D^t_{1500}	NRS-2019	27 (12)
	D^t_{1800}	TR32-2019	66 (8)
val.	D_{day}	WST-2019	30 (9)

small footprints of a few square meters depending on the experimental set-up. Fluorescence estimates derived from FLOX data sets have been used in the past for independent validation of HyPlant SIF estimates (Tagliabue et al., 2019; Krämer et al., 2021).

The present study provides a systematic comparison of SFM, iFLD and SFMNN predictions from HyPlant imagery with FLOX derived iFLD SIF estimates as provided by the manufacturer's processing software. FLOX data sets from 2018–2022 were taken into account. We gained iFLD based FLOX SIF estimates with the processing software provided by the FLOX manufacturer. In order to validate with a consistent data set we disregarded FLOX measurements where the irradiance in the O_2-A band recorded at the beginning and at the end of a measurement cycle varied more than 1% because this is an indicator for changing illumination conditions. The majority of measurements were, however, taken under optimal measurement conditions so that only a negligible number of data points had to be disregarded.

Apart from the SEL-2018 FLOX data set, which was acquired with a mobile FLOX system, the FLOX geolocation was acquired by a separate RTK-GPS measurement. The geolocation for the SEL-2018 FLOX data was derived from UAV data. Due to the high temporal variability of SIF, only FLOX data within ten minutes to a corresponding HyPlant overflight was considered. When multiple FLOX measurements were available within such a ten minute time window, we used the average for comparison with the HyPlant derived predictions, and the variance to compute an uncertainty estimate of the ground SIF measurement.

To account for spatial uncertainties associated with both the geolocation of the in-situ measurements as well as the field of view of single pixels in HyPlant FLUO data, we averaged the SIF prediction in a radius of 1 m, 2 m and 3.4 m for acquisitions acquired 350, 600 and 1150 m above ground level (2 pixel radius), respectively, and used the variance within this region as an uncertainty estimate for the prediction. In addition, we used the variance of multiple FLOX derived SIF measurements collected within the chosen time window of ten minutes as an uncertainty estimate. Both the uncertainties determined for the FLOX measurements and the corresponding uncertainties calculated for the HyPlant derived SIF measurements were used to compute the uncertainty on the mean absolute error (MAE) leveraging first-order error propagation.

2.3. iFLD and SFM airborne SIF estimates

Both SFM and iFLD SIF estimates are generated operationally for all HyPlant campaigns in the O_2-B and O_2-A absorption bands separately. No dedicated rerun of the iFLD and SFM baseline methods was conducted for the comparisons presented in this work. The SFM implementation used for HyPlant FLUO data follows (Cogliati et al., 2019, 2015b) and is applied directly on radiometrically calibrated, but not atmospherically corrected FLUO at-sensor radiances. In this implementation, first a single atmospheric transfer function per acquisition is estimated from the spectral information in barren pixels. Subsequently, a spectral calibration is performed in each pixel to account for sensor miscalibrations. The actual fluorescence estimation is then implemented as a least-squares minimization of the physical radiative transfer model that we have adopted in this contribution as well. In this minimization the model is fitted to radiometrically and spectrally calibrated FLUO at-sensor radiance measurements. It is noteworthy that this implementation of SFM incorporates the atmospheric transfer functions in the at-sensor radiance simulation instead of prior atmospheric correction of the FLUO measurements. A more detailed description of the implementation can be found in Siegmann et al. (2019).

The iFLD implementation for HyPlant FLUO data follows Wieneke et al. (2016) and Damm et al. (2014). Specific implementation details are reported in Siegmann et al. (2019). As the SFM implementation detailed above, this iFLD implementation is applied to radiometrically calibrated, but not atmospherically corrected HyPlant FLUO radiance measurements. A single atmospheric characterization derived with MODTRAN5 is integrated into a set of equations that can be solved analytically. Additionally, the implementation includes an empirical correction term to account for spectral miscalibrations.

3. Development of a novel spectral fitting method

We propose a novel neural-network-based method to predict SIF in the O_2-A absorption band at 760 nm. This approach could principally be adapted to other spectral domains with sensitivity to SIF as well, e.g., at HyPlant spectral resolution the O_2-B absorption band is a-priori suitable as well. The formulation in this contribution focuses on a single contiguous spectral domain (750–770 nm), however, to evaluate the feasibility of the proposed method in a restrained and controlled problem setting where simple modeling the surface reflectance and fluorescence are possible.

The proposed methodology can be regarded as a spectral fitting method (Meroni et al., 2010; Chang et al., 2020) and we call it spectral fitting method neural network (SFMNN), accordingly. Similarly to other spectral fitting methods we first construct an explicit physical model of the measured at-sensor radiance which we then fit to HyPlant at-sensor radiance (L_{HyP}). The prediction of top-of-canopy SIF at 760 nm can be directly derived from the best estimates of the parameters modeling the top-of-canopy fluorescence emission curve.

In contrast to typical spectral fitting methods such as SFM (Cogliati et al., 2015b), where a least-squares minimization is performed, we implement a feature based optimization to fit the model to the observations. Specifically, we train a neural network (see Fig. 2) in a self-supervised fashion using the objective function that is minimized in SFM as a part of the loss formulation. Self-supervised learning means that we do not need SIF ground truth for every training sample, as would be needed for supervised learning. Instead, we use the predicted SIF (as well as predicted reflectance and atmospheric transfer functions) in a physical forward simulation model (the same as used in SFM) to reconstruct the signal. Comparing the reconstructed signal to the input signal allows to evaluate a signal reconstruction error as loss for the usual backpropagation during training of the SFMNN. This loss is complemented with regularizers to ensure a physical disentanglement of atmospheric and surface related contributions to the at-sensor radiance. Training is thus completely independent of any SIF ground

measurements; a fact allowing us to finetune the model to any new data even during prediction where needed or desired.

Differently to SFM, in SFMNN atmospheric transfer functions are estimated locally over small patches which allows to account for changing observation and atmospheric conditions in a straightforward fashion. Moreover, SFMNN relies only on the full HyPlant at-sensor radiance spectrum and a general distribution of high-resolution atmospheric transfer functions. This distribution is gathered from MODTRAN5 atmospheric transfer estimates produced as a side product of SFM applied to a number of HyPlant acquisitions.

3.1. Simulation of HyPlant at-sensor radiance

The loss formulation used for training relies on an explicit forward simulation model of the measured at-sensor signal L_{HyP}, measured over the spectral range $\mathcal{W}_{\mathrm{tot}}$ (670–780 nm), in the spectral subset $\mathcal{W} \subset \mathcal{W}_{\mathrm{tot}}$. The simulation range $\mathcal{W}$ was fixed as the spectral range 750–770 nm covering the O_2-A absorption band. In order to formulate a model for the physical at-sensor signal, we make use of the four-stream forward simulation formulation used in the SFM baseline (Cogliati et al., 2015b), which is based on the Soil Canopy Observation Photosynthesis Energy balance (SCOPE) (van der Tol et al., 2009) radiative transfer model explicitly accounting for diffuse and direct fluxes. It reads

$$\begin{aligned} L_{\mathrm{at-s}} = & \frac{E_s^0 \cos(\theta_s)}{\pi} \\ & \times \left(\rho_{so} + \tau_{oo} \left(\tau_{ss}\, r_{so} + \frac{\tau_{sd} + \tau_{ss}\, \overline{r_{sd}}\, \rho_{dd}}{1 - \overline{r_{dd}}\, \rho_{dd}}\, r_{do} \right) + \tau_{do}\, \frac{\tau_{sd}\, \overline{r_{dd}} + \tau_{ss}\, \overline{r_{sd}}}{1 - \overline{r_{dd}}\, \rho_{dd}} \right) \\ & + \tau_{oo}\, \frac{\left(f + \overline{f_d}\, \rho_{dd}\, r_{do} \right) + \overline{f_d}\, \tau_{do}}{1 - \overline{r_{dd}}\, \rho_{dd}}. \end{aligned} \tag{1}$$

We define all quantities involved in Eq. (1) in Table 3. After rewriting the functions related to atmospheric transfer as $t_0 \dots t_6$ and products thereof as $t_7 \dots t_{12}$ (see Table 3) and simplifying Eq. (1) by setting $r_{sd} = r_{do} = R$, $\overline{r_{sd}} = \overline{r_{dd}} = \overline{R}$, $\overline{f_d} = \overline{f}$ we get

$$\begin{aligned} L_{\mathrm{at-s}} &= L^R_{\mathrm{at-s}} + L^f_{\mathrm{at-s}} \\ &= t_0 \left(t_1 + t_7\, R + \frac{t_8\, R + \overline{R}\, R\, t_{12} + \overline{R}\, (t_9 + t_{10})}{1 - t_2\, \overline{R}} \right) \\ &\quad + \left(t_5\, f_s + \frac{\overline{f}\, (t_6 + t_{11}\, R)}{1 - t_2\, \overline{R}} \right) \end{aligned} \tag{2}$$

where the overline denotes a spatial mean. In practice, this mean is computed by taking the mean over the output window. We estimate $t_1 \dots t_6$, f and R at a high spectral resolution ($\delta\lambda = 0.0055$ nm) by modeling each of these functions in dependency of the input data. The implementation details of the modeling of each of these functions is detailed below in Section 3.2.1.

For the application of the neural network to the HyPlant radiance product L_{HyP}, the simulation model needs to take into account HyPlant's sensor characteristics and potential miscalibrations in addition to the physical process which only yields $L_{\mathrm{at-s}}$. Spectral miscalibration, resulting in smile effects, can lead to a misalignment spectral features in the modeled solar irradiance and atmospheric characterization with respect to the measurements. This can lead to large uninformative gradients in the loss computation described in Section 3.4. In order to simulate L_{HyP}, we need to take into account possible sensor miscalibrations by estimating the shift $\Delta\lambda$ with respect to the nominal wavelength λ and the shift $\Delta\sigma$ with respect to the nominal spectral resolution σ. Optimally, we would consider spectral shifts in each spectral band. Considering the computational overhead resulting from the large number of spectral HyPlant bands that would need to be fitted simultaneously (172 bands), we have restricted the shift prediction. We estimate a single scalar shift $\Delta\lambda$ per spatial pixel and a single shift $\Delta\sigma$ per training set. These shifts do not correspond directly to the physical sensor miscalibration but allow to take into account the effects of spectral miscalibration that otherwise would result in large, uninformative gradients of the loss. Given an estimated center wavelength shift per pixel $\Delta\lambda$, spectral resolution σ and estimated shift in spectral resolution $\Delta\sigma$, a simple sensor model can be created

$$\hat{L}_{\mathrm{HyP}}(\lambda, x, y) = \int_{\mathcal{W}} d\lambda\; g\left(\lambda + (\Delta\lambda)_{x,y} \mid \lambda_i,\, \sigma + \Delta\sigma\right)\; L_{\mathrm{at-s}}\left(\lambda + (\Delta\lambda)_{x,y}, x, y\right) \tag{3}$$

This model gives us the at-sensor radiance as measured by HyPlant $\hat{L}_{\mathrm{HyP}}(\lambda)$ in the spectral range $\mathcal{W}$ (750–770 nm) considered in the simulation. $\hat{L}_{\mathrm{HyP}}$ can be compared to radiometrically calibrated at-sensor radiance $L_{\mathrm{HyP}}(\lambda_i)$ in the nominal center wavelengths λ_i. In practice, we assume a Gaussian Spectral Response Function (SRF) g for all λ_i. This allows us to implement Eq. (3) approximately by Gaussian smoothing followed by a linear interpolation to sample the spectra at nominal HyPlant wavelengths.

Table 3
Definitions for all quantities involved in the simulation model as defined in Eq. (1) and (2).

Eq. (1)	Eq. (2)	Definition
$E_0 \cos(\theta_s)$	t_0	solar irradiance modulated by the local solar zenith angle
f		directional fluorescence emission
$\overline{f_d}$	$\overline{f}$	diffuse fluorescence emission
ρ_{so}	t_1	bi-directional atmospheric reflectance
ρ_{dd}	t_2	spherical albedo at the bottom of the atmosphere
τ_{oo}	t_3	directional atmospheric transmittance along observation direction
τ_{ss}	t_4	directional atmospheric transmittance in solar direction
τ_{do}	t_5	directional atmospheric transmittance in observation direction for diffuse incidence
τ_{sd}	t_6	diffuse transmittance for solar incidence
r_{so}	R	bi-directional reflectance factor (BRF)
r_{do}	R	hemispheric-directional reflectance factor (HDRF)
$\overline{r_{dd}}$	$\overline{R}$	bi-hemispherical reflectance factor (BHRF) of the surrounding
$\overline{r_{sd}}$	$\overline{R}$	directional-hemispherical reflectance factor (DHRF) of the surrounding
$\tau_{ss}\, \tau_{oo}$	t_7	multiplication definitions in Eq. (2)
$\tau_{sd}\, \tau_{oo}$	t_8	
$\tau_{ss}\, \tau_{do}$	t_9	
$\tau_{ss}\, \rho_{dd}$	t_{10}	
$\tau_{oo}\, \rho_{dd}$	t_{11}	
$\tau_{ss}\, \rho_{dd}\, \tau_{oo}$	t_{12}	

3.2. Architecture

SFMNN acts on patches of spatially contiguous spectral input $c_{xy} \in \mathbb{R}^{p \times p \times (\Lambda + N_p)}$, where p denotes the spatial patch dimension, $\Lambda = 1024$ the spectral dimensionality of the full spectral range of the FLUO sensor $\mathcal{W}_{\mathrm{tot}}$ and $N_p = 3$ the number of additional variables passed to the network (nominal flight height, solar zenith angle, across-track position). We randomly draw these patches from all the acquisitions in the data set during training. The patch's dimensions p were fixed in all experiments in this work. Preliminary experiments have shown patches of 17×17 pixels to allow training batch sizes that were sufficiently large for efficient training and to constrain the optimization. While

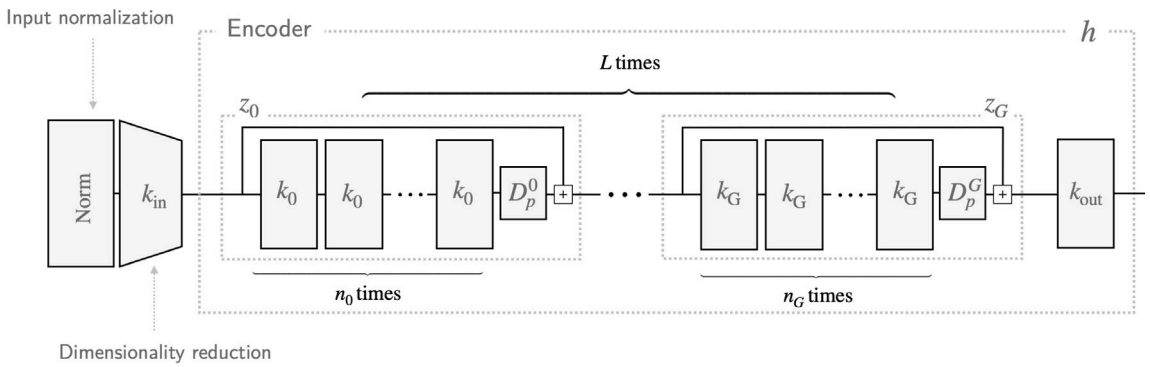

Fig. 3. Conceptual sketch of the concatenation of input normalization layer, dimensionality reduction and encoder architecture h.

we have fixed the patch size in all experiments, further investigations should consider varying this patch size as a function of the physical pixel size, i.e. the sensor flight height. This input consists of the full spectral range of the FLUO at-sensor radiance where each band is interpreted as a channel to the neural network. In addition to the spectral input we also add the nominal flight height, the solar zenith angle and the spatial across-track position as additional layers to the input patch. All parameters are predicted in a pixelwise fashion except parameters of the atmospheric functions t_i and $\Delta\sigma$. The atmospheric functions t_i are estimated on a patchwise basis to enforce the empirical expectation of large auto-correlation distances of atmospheric parameters. $\Delta\sigma$ was estimated directly as a network parameter since preliminary experiments have shown that formulating it as a function of the spectral input would affect disadvantageously the decomposition capacity of the network. SFMNN consists of a normalization layer, a dimensionality reduction layer k_{in}, an encoder e_{in} and several decoder modules for each of the variables. Both e_{in} and the decoder modules are simple multi-layer perceptrons with residual links.

The spatially dependent input c_{xy} passed to SFMNN is first normalized as presented in Fig. 3, where we show the first layers of SFMNN. The normalization layer is implemented as a batch normalization layer that is trained with the network during one epoch. In order to decrease the large input dimensionality of 1027 channels (1024 spectral channels and 3 additional variables), we introduce a dimensionality reduction to 100 channels implemented as a linear layer followed by a rectified linear unit (ReLU) activation (k_{in} in Fig. 3).

The construction of the prediction network involves transforms k_i simply defined as

$$k_{\text{i}} : \text{ReLU} \circ \text{BN} \circ \ell_{k_{i-1}\to k_i} \tag{4}$$

where $\ell_{k_{i-1}\to k_i}$ is a linear layer with input and output dimensions d_{i-1} and d_i, BN denotes a batch normalization layer (Ioffe and Szegedy, 2015; Wu and He, 2018) and ReLU a rectified linear unit. Both encoder e_{in} and decoder modules are defined as h modules with differing layer dimensions listed in Table 4. We define a module h as $k_{\text{out}} \circ z_L \circ \ldots \circ z_0$ with

$$z_i(x) = \text{D}_p^i \circ \text{BN} \circ \text{ReLU} \circ \left(\ell_{k_{i-1}\to k_i}(x) + \left(k_i \circ \ldots \circ k_i\right)(x)\right) \tag{5}$$

implementing the repeated application of layers k_i and a residual link. D_p^i denotes a dropout layer with dropout probability p. k_i are defined as in Eq. (4). The dimensions of the linear layers of all submodules of e_{in} are listed in Table 4.

3.2.1. Mapping the decoded input spectra to physical parameters

Decoder modules are constructed identically to the encoder e_{in}, i.e. they are implemented as h modules but with submodules of different dimensions as compared to e_{in}. We list all the dimensions of the decoder module in Table 4. All decoders act on the same spatially dependent encoding $p_{xy} = e_{\text{in}}(c_{xy})$ of the input c_{xy}. Each decoding $q_v = d_v(p_{xy})$ for variable v is then mapped to the physical parameters in Eq. (2). The mapping between the decoder outputs q_v and the physical values of variables that are predicted in a pixelwise fashion is implemented by a scaling layer

$$m(q \mid b_\ell, b_u) = b_\ell + \text{sigm}\,(q)\left(b_u - b_\ell\right) \tag{6}$$

where sigm denotes the sigmoid function. This formulation restricts the solution space to predefined parameter ranges (b_ℓ, b_u). These parameter ranges were chosen according to prior knowledge and are listed in Table 5.

We allow scalar and spatially variable $\Delta\lambda$ across acquisitions and different campaigns. We include this variation in the forward simulation by constructing a decoder $d_{\Delta\lambda}$ with a scaling layer

$$d_{\Delta\lambda}(p) = m\left(d(p) \mid \left(b_{\Delta\lambda}\right)_\ell, \left(b_{\Delta\lambda}\right)_u\right) \tag{7}$$

Similarly, we construct the decoder $d_f(p) \to (A_f, \sigma_f)$ that yields the parameterization for the top-of-canopy fluorescence emission. Since the present contribution is restricted to SIF estimation in the O_2-A absorption band, we restrict the model to the emission peak at 737 nm. We assume a normal distribution for

$$f(\lambda) = A_f\, \mathcal{N}\left(\lambda \mid \mu_\lambda, \sigma_f\right),\ \lambda \in \mathcal{W} \tag{8}$$

around the emission peak $\mu_f = 737$ nm similarly to Pato et al. (2023), Subhash and Mohanan (1997). While more precise functional expressions for top-of-canopy fluorescence have been proposed (Cogliati et al.,

Table 4
Architecture dimensionalities according to Fig. 3. Each element in a tuple denotes an architecture parameter for the ith encoder or decoder layer ($0 \le i \le G$). k_i denotes the dimensionality of the ith encoder (decoder) sublayers, n_i denotes the number of repetitions of sublayers, D_p^i denotes the dropout rate of the output of the ith encoder (decoder) layer.

	k_i	n_i	D_p^i
Encoder e_{in}	(100, 50, 50)	(3, 3, 1)	(0.1, 0)
Decoder d_v	(100, 50, 50, 50)	(3, 1, 1, 1)	(0, 0, 0, 0)

Table 5
Upper and lower bounds parameterizing the scaling layers for each variable needed in the signal reconstruction. ρ, s_ρ and e parameterize the reflectance (see Eq. (9)), A_f and σ_f parameterize the fluorescence signal model (see Eq. (8)), $\Delta\lambda$ denotes the maximum wavelength shift per band (see. Eq. (7)), E and t denote the maximum range of the estimated atmospheric transfer PCA weights (see Eq. (10)) and the solar irradiance variation (see Eq. (11)).

	ρ	s_ρ	e	A_f	σ_f	$\Delta\lambda$	E	t
Lower bound b_ℓ	0	0	0	0	20	−0.09	0.98	−300
Upper bound b_u	0.6	12×10^{-3}	1	8	21	0.09	1.02	300

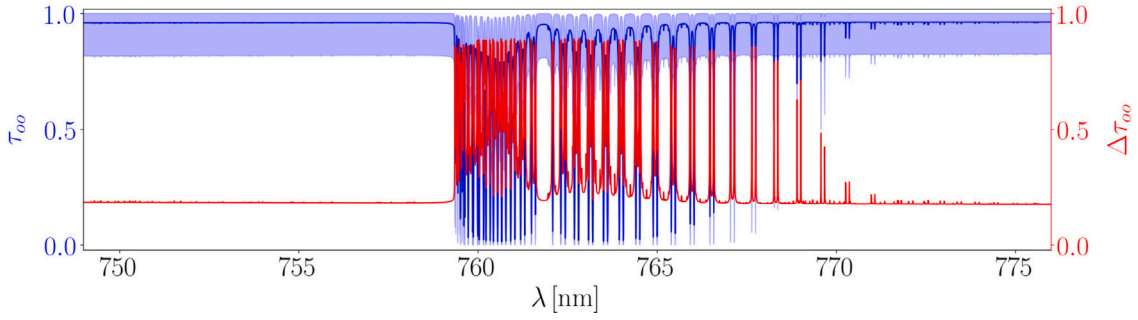

Fig. 4. Distribution of the SFM estimated transfer function τ_{oo} used for the PCA decomposition in shaded blue. We show the lower and upper bound as well as the mean τ_{oo} . The total extent of $\Delta\tau_{oo} = \max(\tau_{oo}) - \min(\tau_{oo})$ in the selected data set is shown in red. (For interpretation of the references to color in this figure legend, the reader is referred to the web version of this article.)

2015b; Magney et al., 2019) we adopt here the normal distribution for simplicity. We expect the errors incurred from the model mismatch to be marginal as the spectral reconstruction is restricted to a narrow spectral range $\mathcal{W}$. The prediction bounds parameterizing the scaling layer are given in Table 5.

Equivalently, we restrict the definition of the reflectance R to a region covering tightly the simulated spectral range around the O_2-A absorption band $\mathcal{W}$. We assume R can be approximately expressed by a square polynomial in this spectral range. Following (Pato et al., 2023, 2024) a network $d_R(p) \rightarrow (\rho, s_\rho, e)$ is constructed in a way that reflectance estimates can be written

$$R(\lambda \mid p) = \rho + s_\rho(\lambda - \lambda_0) + \frac{s_\rho(e-1)(\lambda-\lambda_0)^2}{2(\lambda_1 - \lambda_0)}, \ \lambda \in \mathcal{W} \tag{9}$$

where we define $\lambda_0 = 740$ nm and $\lambda_1 = 780$ nm. The bounds of the scaling layer for ρ, s_ρ and e are given in Table 5. It has proven to allow a physiologically consistent parameterization of observed reflectance spectra.

Lastly, we highlight that we estimate a single FWHM shift $\Delta\sigma$ for the whole training data set, contrarily to the CW shifts $\Delta\lambda$ and fluorescence and reflectance parameters which are estimated for each pixel. $\Delta\sigma$ is estimated as a single free parameter in the network. We chose this simplification of the retrieval problem as preliminary analysis has shown that any larger degree of freedom in the prediction of $\Delta\sigma$ impacted the fluorescence retrieval negatively.

3.2.2. Atmosphere estimation

We predict the atmospheric functions $t_1, \ldots, t_6$ and calculate the products $t_7, \ldots, t_{12}$ defined in Eq. (2). Differently to SFM, we do not rely directly on MODTRAN simulations to estimate the atmospheric transfer. Instead, we perform a Principal Component Analysis (PCA) decomposition on a chosen set of MODTRAN simulated atmospheric functions that were derived by SFM for a range of different HyPlant acquisitions (see Fig. 4). Since HyPlant flights are operated under comparable weather conditions, we assume that we can find fitting atmospheric functions for arbitrary HyPlant acquisitions in the span of the first five PCA components. This procedure is similar to Joiner et al. (2013, 2016) where atmospheric transfer estimates are derived from linear interpolations over a decomposition of the expected space of possible atmospheric transfer functions.

In order to derive a suitable PCA decomposition we used high resolution (0.0055 nm) atmospheric transfer functions calculated during SFM optimization for 38 acquisitions from a compilation of acquisitions from 2018 and 2019 (Rascher et al., 2021, 2022a). Fig. 4 shows as an example the distribution of the SFM estimated transfer function τ_{oo} in these selected acquisitions. These acquisitions were chosen to cover a multitude of flight heights, flight directions, and day times to ensure that the span of the PCA components covers all acquisitions considered in this work. We show the distribution of atmospheric conditions for these transfer functions in Fig. 5(a) and (b).

We highlight that we included atmospheric transfer functions of SEL-2018 and WST-2019 acquisitions, which are also used for training and validation (see Table 1) in this data set. In the case of acquisitions from these two campaigns we thus guarantee that the SFM solution for the atmospheric transfer functions is in the solution space of SFMNN's atmospheric predictor.

We derived the first five principal components g_{ij} from all distributions of $t_1, \ldots, t_6$ before training the network. These components g_{ij} (with $1 \leq i \leq 6$ and $0 \leq j \leq 5$) and according means μ_i and standard deviations σ_i were then used for all experiments. In order to estimate PCA weights from the encoded HyPlant radiance input p, we construct networks $d_{t_i}(p) \rightarrow \{q_{ij}\}_{j \leq N_c}$ such that

$$t_i(p) = \min\left(1, \mu_i + \sigma_i \sum_{j \leq N_c} g_{ij} w_{ij}\right), \text{ with } w_{ij} = m\left(q_{ij} \mid (b_t)_\ell, (b_t)_u\right) \tag{10}$$

where p is the single pixel encoding as defined above and $N_c = 5$ is the number of components used for the PCA reconstruction.

To test our assumption that atmospheric functions under typical HyPlant operation conditions may indeed be approximated by a PCA reconstruction, we show in Fig. 5 the results of a k-fold cross-validation where we evaluate the reconstruction error of each atmospheric function $t_1, \ldots, t_6$ in HyPlant spectral resolution. The reconstruction is performed using the first five components derived from 50% subsets. We draw these subsets randomly 50 times and establish optimal reconstruction weights using a least-squares minimization of the absolute error on the remaining 30% of the atmospheric functions at our disposal. From this analysis it becomes clear that almost all transfer function have a weight representation with approximation errors of less than 2% in terms of normalized absolute errors (nMAE). The reconstructions of ρ_{so} and, to a lesser degree, of τ_{do} yield nMAE 2%–10%. These approximation errors make our method less precise. Particularly, diffuse conditions may not be well represented by our atmospheric model as a consequence.

Optimally a larger data base of atmospheric transfer functions would be chosen to derive suitable PCA components to the atmospheric part of our model. We show in the following results based on a PCA decomposition derived from this small data set of 38 sets of atmospheric transfer functions and can show that it is sufficient to yield comparable SIF retrieval performance to SFM and iFLD on our in-situ validation data set.

Finally, for the solar top-of-atmosphere (TOA) irradiance t_0 we predict a single weight q_0 for the whole training dataset and use the solar irradiance spectrum E_s^0 (Kurucz, 2006) modulated by the true

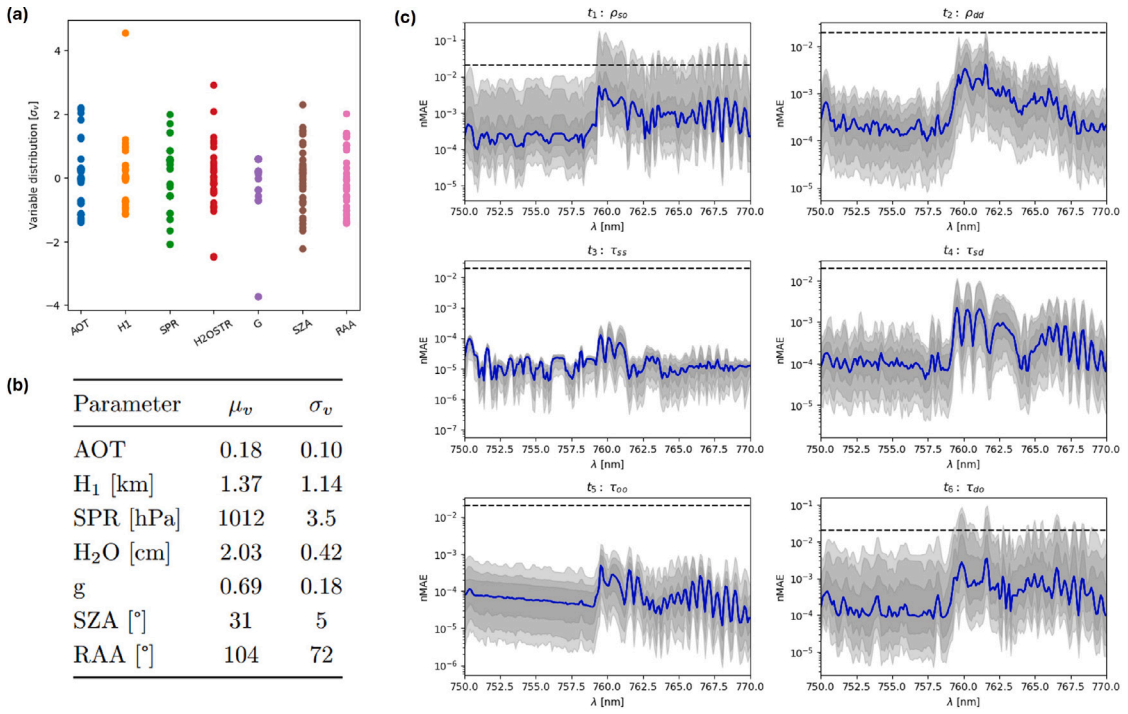

Parameter	μ_v	σ_v
AOT	0.18	0.10
H_1 [km]	1.37	1.14
SPR [hPa]	1012	3.5
H_2O [cm]	2.03	0.42
g	0.69	0.18
SZA [°]	31	5
RAA [°]	104	72

Fig. 5. (a) and (b): Distribution of atmospheric conditions of atmospheric transfer functions used to derive the PCA-based atmospheric model. *AOT* denotes the aerosol optical thickness at 550 nm, H_1 the flight height above sea level, *SPR* the atmospheric surface pressure, H_2O water vapor content, *g* the scattering anisotropy factor, *SZA* the solar zenith angle and *RAA* the relative azimuth angle between sun and sensor. **(c):** K-fold cross-validation results of the PCA-reconstruction. We plot the normalized mean absolute error (nMAE) between target and reconstructed transfer function. Gray scales denote the 5%–95%, 10%–90% and 25%–75% percentiles and blue the median. Dashed lines denote 2% as a reference. For variable definitions see Table 3. (For interpretation of the references to color in this figure legend, the reader is referred to the web version of this article.)

solar zenith angle θ_s corresponding to the acquisition time and location as initial guess for the solar irradiance at acquisition time from which the network is allowed to deviate slightly, i.e.

$$t_0 = E_s^0 \cos(\theta_s) \left((b_E)_\ell + \mathrm{sigm}(q_0) \left((b_E)_u - (b_E)_\ell \right) \right). \tag{11}$$

Here, q_0 is a free parameter and does not depend on the spectral input p since we introduce possible deviation from the solar irradiance E_s^0 (Kurucz, 2006) only to account for (i) a possible model mismatch and (ii) miscalibration of radiometrically calibrated HyPlant FLUO radiance. Since t_0 is supposed to be constant, the bounds $(b_E)_\ell$ and $(b_E)_u$ are chosen tightly. Simultaneous training over acquisitions recorded over time frames that do not allow the assumption of a constant solar TOA irradiance would have to account for the variability of E_s^0 by using precise daily E_s^0 estimates.

3.3. Architectural constraint

The architecture of $d_{t_i}(p)$ differs from the decoder structure introduced before, because we require a single prediction t_i per patch and not per pixel. This is necessary since we architecturally constrain the ill-posed retrieval by requiring the atmospheric prediction to hold over an extended spatial domain. We implement this by first averaging a per-pixel atmosphere encoding $d_{t_i}(p)$ over the patch. $d_{t_i}(p)$ is architecturally identical to d_f and d_R. Thus, we estimate q_i as

$$q_i = \mathrm{BN} \circ \ell_{d_a \to N_c} \circ \sum_{x,y \le s} s^{-2} d_{t_i}(p_{xy}) \tag{12}$$

where $\ell_{d_a \to K}$ is a linear layer with input and output dimensions d_a and N_c, where s is the number of pixels per side of a square patch in across-track dimension x and along-track dimension y and where BN denotes a batch normalization layer.

3.4. Loss & regularization

We formulate the following unsupervised loss per patch for the SIF regression problem for the spectral domain $\mathcal{W}$

$$\ell(L_{\mathrm{HyP}}, \hat{L}_{\mathrm{HyP}}) = (\ell_{\mathcal{W}} + \gamma_f \ell_f + \gamma_N \ell_{\mathrm{NDVI}} + \gamma_a \ell_{\mathrm{atm}})(L_{\mathrm{HyP}}, \hat{L}_{\mathrm{HyP}}), \tag{13}$$

where γ_f, γ_N and γ_a are weighting factors that fix the relative importance of individual loss terms. These values were fixed in preliminary experiments as $\gamma_f = 5$, $\gamma_N = 10$ and $\gamma_a = 1$ as they yielded a small difference between SFMNN and SFM SIF predictions in preliminary tests with an individual acquisition (WST 16/06/2019 11:28). Varying these weights adjusts the importance of individual loss components. No thorough validation over the sensitivity of the proposed method with respect to these values has been conducted, however.

This loss implements a least-squares minimization on the measured at-sensor radiance. It is composed of the main loss contribution over the spectral range $\mathcal{W}$ (750–770 nm)

$$\ell_{\mathcal{W}} = |\mathcal{W}|^{-1} \mu \left(\sum_{\lambda \in \mathcal{W}} \left(L_{\mathrm{HyP}}(\lambda) - \hat{L}_{\mathrm{HyP}}(\lambda) \right)^2 \right), \tag{14}$$

where μ denotes the mean over all pixels. The three additional signal ℓ_f, physiological ℓ_{NDVI} and physical ℓ_{atm} regularizers account for data-specific constraints.

3.4.1. Signal regularization

The regularizer

$$\ell_f = |\mathcal{W}|^{-1} \mu \left(\sum_{\lambda \in \mathcal{W}} w_f(\lambda) \left(L_{\mathrm{HyP}}(\lambda) - \hat{L}_{\mathrm{HyP}}(\lambda) \right)^2 \right)_{\delta \mathrm{R} = \delta \mathrm{t}_{\mathrm{atm}} = 0} \tag{15}$$

weights the reconstruction with a sensor and signal specific weight function w_f. w_f boosts the loss in spectral regions with high fluorescence SNR. The gradient computation of ℓ_f is set to only influence the fluorescence module d_f as the definition of w_λ assumes known reflectance and atmospheric transfer functions.

We define w_f as the Moore–Penrose solution to a simplified and linearized retrieval problem. The derivation of the linearized problem and these weights (see Appendix) result in the definition

$$w_f(\lambda) = \left\langle \frac{1}{u_\lambda^2} \frac{\sum_{\lambda'} f_{\lambda'}^2}{\sum_{\lambda'} f_{\lambda'}^2 / u_{\lambda'}^2} \right\rangle_{p(L_{\text{at-s}}, f)} \tag{16}$$

where f denotes the predicted at-sensor fluorescence, u_λ the estimated sensor variance of $L_{\text{at-s}}$ and $\langle \dots \rangle_{p(L_{\text{at-s}}, f)}$ the expectation over a representative distribution of at-sensor radiance and fluorescence emission. We show the mean weights w_f used in all experiments that we estimate using a fixed distribution $p(L_{\text{at-s}}, f)$ in Fig. 1. Both the variability of w_f as well as the influence of w_f on the learned retrieval have not been investigated in this work.

3.4.2. Physiological constraint

The regularizer

$$\ell_{\text{NDVI}} = \mu \left(\hat{f} \, \delta \left(\text{NDVI} \leq \tau_{\text{NDVI}} \right) \right) \tag{17}$$

was introduced to reinforce the physiological expectation of vanishing fluorescence in sparsely vegetated areas. In Eq. (17) the prediction network's fluorescence prediction at 760 nm, $\hat{f}$, is evaluated in pixels with low vegetation cover as expressed by a threshold on NDVI, τ_{NDVI}. We fixed $\tau_{\text{NDVI}} = 0.15$ in all experiments in accordance with a similar thresholding principle in SFM (Cogliati et al., 2019). The NDVI is derived online during training and inference from the FLUO input spectra.

3.4.3. Physical regularization

For practical purposes, we define the total effective predicted transfer function with respect to the direct solar irradiance

$$t_{\text{tot}} = \frac{L_{\text{at-s}}^R \, \overline{R}^{-1}}{E_s^0 \cos(\theta_s)} \tag{18}$$

describing both downwelling, upwelling and diffuse contributions to the at-sensor signal. In this computation, we only use the reflectance signal contribution $L_{\text{at-s}}^R$ from Eq. (2). We point out that the resulting effective transfer function t_{tot} may not respect $\max(t_{\text{tot}}) < 1$ because of diffuse contributions to the at-sensor signal even though individual components $t_1 \dots t_6$ are constrained to < 1. This is caused by the definition of t_{tot} which relates only to the direct solar irradiance. The additional diffuse downwelling and upwelling contributions in the simulation model used in this work are not part of the normalizing denominator and can, thus, lead to $t_{\text{tot}} > 1$. We can assume the diffuse components to the measured at-sensor radiance to be small under typical HyPlant observation conditions. We make sure that the atmospheric transfer functions result in a physically plausible total transfer function t_{tot} that is not much larger than 1. by regularizing the loss with a soft constraint to enforce $\text{ReLU}(t_{\text{tot}} - 1)$ to be small.. Thus, we add

$$\ell_{\text{atm}} = \text{ReLU}(t_{\text{tot}} - 1) \tag{19}$$

as an additional regularizer to the loss. It constrains the network to decrease diffuse parts of the predicted atmospheric transfer. While this regularizer achieves the soft constraint with a suitable weight γ_a in the loss (see Eq. (13)), it has the downside that the fixed hyperparameter γ_a effectively controls the contribution of simulated diffuse at-sensor radiance.

3.5. Training set up

The training of the SFMNN network was conducted in two phases. First we performed a pretraining on a data compilation of acquisitions from different nominal heights $\mathcal{D}_{\text{mix}}$ (cf. Table 1). This pretraining provided us with a coarsely trained network p_{mix}, which we then fine-tuned to gain predictors for specific observation and terrain conditions. We trained networks p_{350}, p_{600} and p_{1500} for individual nominal flight heights (350, 600 and 1500 m) in flat terrain. In Table 1 we detail the composition of the corresponding compilations $\mathcal{D}_{350} \dots \mathcal{D}_{1500}$ that were used for fine tuning. In addition to the flat terrain predictors, we also compiled data sets with variable topography ($\mathcal{D}^t_{600}$, $\mathcal{D}^t_{1150}$, $\mathcal{D}^t_{1500}$ and $\mathcal{D}^t_{1800}$). Due to a significantly reduced availability of HyPlant data in topographically complex terrain these compilations mainly consist of acquisitions from a single campaign.

The HyPlant acquisitions in a training data set were cut spatially in partially overlapping patches. A fixed patch size of 17 × 17 HyPlant pixels was chosen. While we used the whole spectral range covered by the FLUO module as spectral input window $\mathcal{W}_{\text{tot}}$, we restricted the prediction range to the more constrained simulation range $\mathcal{W} = [750, 770]$ nm. A larger simulation range would have required modeling of the at-sensor radiance in a larger spectral domain. Since this work focuses on the O_2-A absorption band we instead restricted the fluorescence estimate to 750–770 nm while still allowing the network to leverage information on the fluorescence emission outside the spectral window which we simulate. In all training runs, the input provided to the network consisted of concatenated layers of the spectral information, the across-track pixel location as well as the mean solar incidence angle per acquisition. With respect to the analysis of predicted transfer functions in topographically variable terrain, we point out that no topographic elevation such as a digital elevation model (DEM) was provided to SFMNN during training or testing time.

The training was conducted with an Adam optimizer guided gradient descent Kingma and Ba (2017). The nominal learning rate was set initially to $\ell_r = 10^{-3}$ and subsequently reduced to a minimum of $\ell_r = 10^{-4}$ with a learning rate scheduler. All networks (p_{mix}, $p_{350} \dots$) were trained until the validation loss on a random subset of the training data stopped decreasing.

4. Results

In order to validate the SFMNN reconstruction and retrieval performance, we present a qualitative comparison of the reconstructed at-sensor radiance of SFM and SFMNN as well as a quantitative comparison of SFMNN top-of-canopy fluorescence estimates against top-of-canopy FLOX measurements. Additionally, we include two application studies to assess the physiological and physical plausibility of SFMNN's estimated parameters.

4.1. At-sensor radiance reconstruction performance

Good reconstruction performance of the at-sensor radiance is a critical prerequisite for successfully disentangling R, f and the atmospheric transfer functions t_i. In order for SFMNN to yield consistent SIF estimates, comparable reconstruction performance across a wide range of observational conditions is needed. While, the reconstruction is an important evaluation metric, it does, however, not guarantee the correctness of the estimated at-sensor signal decomposition. This is due to the ill-posed nature of this decomposition problem that may allow ambiguous solutions resulting in similarly small residuals.

We show that SFMNN reaches a reconstruction performance similar to SFM by analyzing error statistics of the predicted at-sensor radiance both in the full simulation range $\mathcal{W}$ (750–770 nm) as well as in the spectral range $\mathcal{W}_{O_{2-A}} = [759.55, 761.60]$ nm in the O_2-A absorption band. In Fig. 6 we plot the 5%–95% percentiles of the absolute reconstruction residuals along with the mean absolute

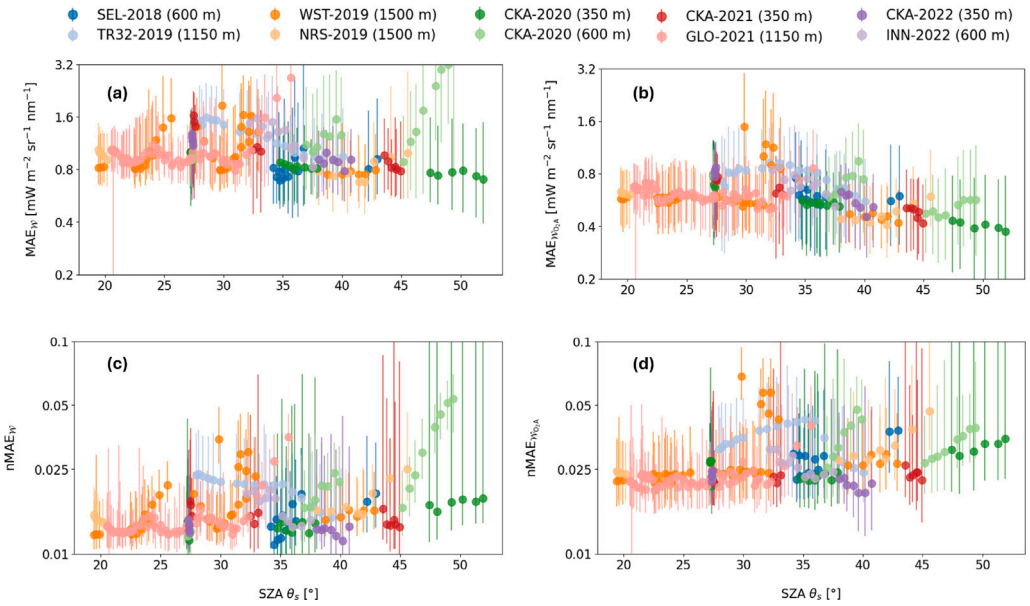

Fig. 6. Statistics of absolute errors across single acquisitions. We show the mean 5, 50 and 95% quantiles of absolute error (MAE, upper row) and of normalized absolute error (nMAE, lower row) between observed radiance and radiance predicted by SFMNN in the spectral ranges $\mathcal{W} = [750, 770]$ nm (*(a)* and *(c)*) and $\mathcal{W}_{O_2\text{-}A} = [759.55, 761.60]$ nm (*(b)* and *(d)*) as a function of the sun zenith angle (SZA). (For interpretation of the references to color in this figure legend, the reader is referred to the web version of this article.)

error (MAE). The SFMNN simulations exhibit overall mean absolute error ($\text{MAE}_{\mathcal{W}}$) distributions constrained consistently in the range 0.6–2 mW nm^{-1} sr^{-1} m^{-2} (Fig. 6(a)) and $\text{MAE}_{\mathcal{W}_{O_2A}}$ in the O_2-A band in the range 0.4–1 mW nm^{-1} sr^{-1} m^{-2} (Fig. 6(b)). We equally show the normalized mean absolute error distributions

$$\text{nMAE}_{\mathcal{W}} = \frac{\left|\hat{L}_{\text{HyP}} - L_{\text{HyP}}\right|}{L_{\text{HyP}}} \tag{20}$$

for the spectral range $\mathcal{W}$ in Fig. 6(c) and equally for $\mathcal{W}_{O_2A}$ in (d). Contrarily to the MAE, we find increasing nMAE outliers with increasing SZA. The MAE decreases more slowly than the mean at-sensor radiance with increasingly diffuse conditions for image data acquired under high SZA. As a consequence, the nMAE increases under low-light conditions.

In order to assess whether SFMNN's reconstruction error is sufficient for a spectral fitting based SIF retrieval, we compare the reconstruction residuals of SFMNN and the SFM baseline. The present study only focuses on a comparison in the D_{day} dataset. To highlight the variability in reconstruction performance across different light regimes we differentiate between *noon* acquisitions taken around the solar noon (13:15, 13:30, 13:38 CEST) and *off-noon* acquisitions taken in the morning and afternoon (10:11, 10:19, 10:27, 10:34, 16:11, 16:18 CEST).

In Fig. 7(a) and (b) we plot the mean absolute error distributions $\text{MAE}_{\mathcal{W}}$ over simulation range $\mathcal{W}$ (750–770 nm) and $\text{MAE}_{\mathcal{W}_{O_2\text{-}A}}$ in the O_2-A band (759.55–761.60 nm). SFMNN's reconstruction performance over the full spectrum (see Fig. 7(a)) is sightly worse than SFM. Contrarily, in the O_2-A band (see Fig. 7(b)) we see an improvement of SFMNN over SFM. In both cases, we find lower reconstruction errors in *off-noon* than in *noon* acquisitions, but increased nMAE in *off-noon* consistent with the discussion of Fig. 6 above. This partially improved performance of SFMNN over SFM in the O_2-A band of in the D_{day} data set can also be observed in terms of $\text{nMAE}_{O_2\text{-}A}$ in 7 (c) and (d). As for the absolute MAE, we find worse overall performance $\text{nMAE}_{\mathcal{W}}$ but an improvement of SFMNN in the O_2-A band.

We conclude that SFMNN is able to learn a reconstruction of the at-sensor radiance with a reconstruction error in the O_2-A band consistently bounded in the range 0.4–1 mW nm^{-1} sr^{-1} m^{-2} over the whole range of observational conditions covered by the data sets. SFMNN's prediction accuracy in the O_2-A band is improved over the operational SFM predictions in the D_{day} dataset both in terms of MAE and nMAE, but falls short of SFM's performance when comparing residuals in the full simulation range $\mathcal{W}$ in off-noon conditions.

4.2. Validation of SFMNN predicted top-of-canopy fluorescence with FLOX measurements

In order to evaluate whether SFMNN's decomposition of the at-sensor radiance yields SIF estimates comparable to SFM and iFLD baselines, we directly validate SFMNN SIF with in-situ SIF measurements that were acquired quasi-simultaneously to the airborne HyPlant acquisitions. In particular, we compare FLOX derived iFLD SIF estimates to HyPlant derived SIF predictions for the five measurement campaigns SEL-2018 (600 m), WST-2019 (1500 m), CKA-2020 (350 m), CKA-2020 (600 m), CKA-2021 (350 m), GLO-2021 (1150 m) and CKA-2022 (600 m) (see Table 2). We show comparative scatter plots (Fig. 8) and performance metrics of HyPlant derived SFM, SFMNN and iFLD (Table 6) taking into account all in-situ FLOX measurements available after filtering as described in Section 2.2. In addition to the MAE, the results report the Pearson correlation r.

The validation results show that SFMNN outperforms the two baseline methods in terms of r for all but two datasets (see Table 6). In these two data sets providing a lower validation accuracy, CKA-2020 (350 m) and CKA-2021 (350 m), r is still close to the best performing baseline method. A similar conclusion can be drawn when comparing the performance in terms of mean absolute error (MAE). While the MAE of SFMNN suffers from bias leading to overestimation in all datasets it ranks at least second in all but one dataset (CKA-2021 (350 m)) The overall validation results in Table 6 and the scatter plots in Fig. 8 suggest that SFMNN has the strongest sensitivity to changes in in-situ measured SIF, but that the prediction bias leads to a underperformance with respect to iFLD and SFM in terms of MAE.

The results for the CKA-2020 (350 m) and (600 m) runs refer to data acquired by three different FLOX systems placed in two different crop types (winter wheat, oat). In order to avoid biased metrics due to sensor specific and crop type phenological differences that potentially influenced the FLOX measurements, we additionally list the prediction performance over the measurement series of the individual measurement stations at the ground (see Table 7). The results in Table 7 show that there is variation in the performance metrics across the

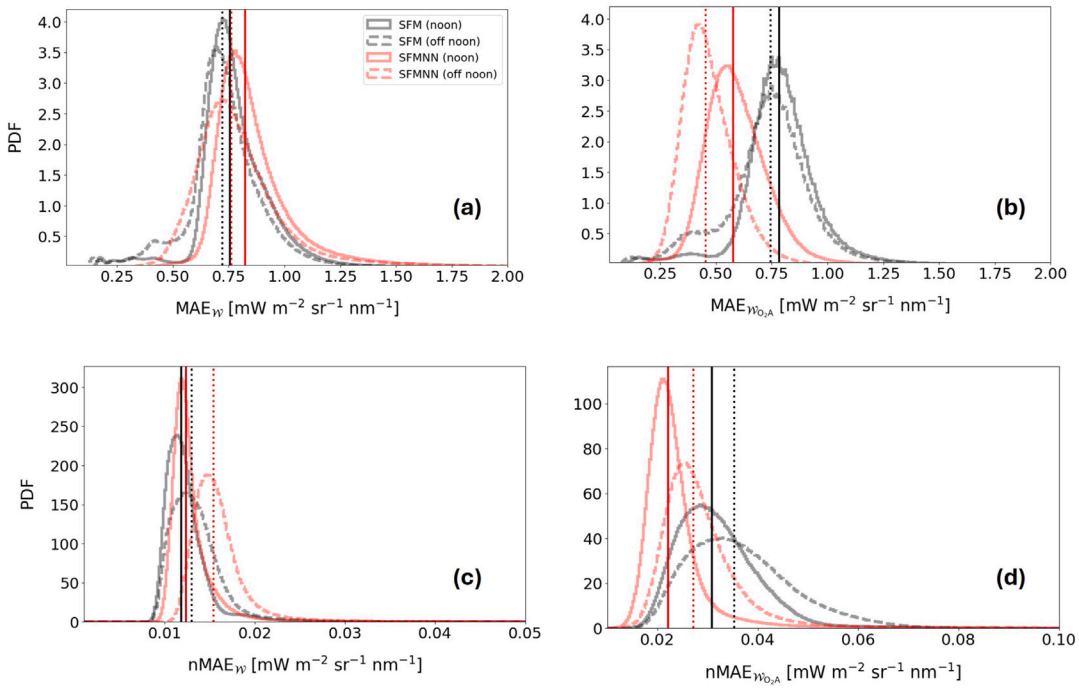

Fig. 7. Residual distribution of SFM and SFMNN reconstructions of WST-2019 (1500 m) acquisitions sampling a single day (2019/06/19). *noon* denotes data from 12:00–14:00 (3 acquisitions), *off-noon* denotes data acquired earlier than 12:00 or later than 14:00 (6 acquisitions). Shown are (a) absolute error distributions MAE$_{\mathcal{W}}$ over the complete spectral window $\mathcal{W}$, (b) MAE$_{\mathcal{W}_{O_2A}}$ in the O_2-A band [759.55, 761.60] nm and corresponding normalized absolute error distributions (c) nMAE$_{\mathcal{W}}$ and (d) nMAE$_{\mathcal{W}_{O_2A}}$ as defined in Eq. (20). (For interpretation of the references to color in this figure legend, the reader is referred to the web version of this article.)

Table 6
FLOX derived SIF measurements compared to SFMNN, SFM and iFLD SIF predictions (≤10 min time difference). Correlation r marked with * have $p > 0.05$. Mean absolute errors (MAE) are given in mW nm^{-1} sr^{-1} m^{-2}. N denotes the number of validation points. We highlight the best results in bold font. Multiple MAE results are highlighted, if the uncertainty is too large to establish a single *best* case. All uncertainties are computed from the variation of HyPlant derived SIF estimates within a fixed radius (350 m: 0.5 m, 600 m: 1 m, 1150 m: 2 m) around the measurement location and the variation of FLOX SIF estimates within the predefined time window of 10 min.

Data set		r	MAE	N
SEL-2018 (600 m)	SFM	0.81	0.82 ± 0.12	9
	SFMNN	**0.96**	0.68 ± 0.08	11
	iFLD	0.78	**0.58 ± 0.09**	10
WST-2019 (1500 m)	SFM	−0.35*	0.48 ± 0.07	22
	SFMNN	**0.58**	**0.20 ± 0.08**	22
	iFLD	−0.12*	0.78 ± 0.09	18
CKA-2020 (600 m)	SFM	**0.83**	0.42 ± 0.05	23
	SFMNN	**0.83**	**0.29 ± 0.05**	23
	iFLD	0.52	0.39 ± 0.08	23
CKA-2020 (350 m)	SFM	**0.90**	0.36 ± 0.04	37
	SFMNN	0.86	0.35 ± 0.04	37
	iFLD	0.55	**0.28 ± 0.05**	36
GLO-2021 (1150 m)	SFM	0.89	**0.24 ± 0.09**	6
	SFMNN	**0.91**	0.38 ± 0.15	6
	iFLD	0.81	0.73 ± 0.14	6
CKA-2021 (350 m)	SFM	0.64*	0.44 ± 0.07	7
	SFMNN	0.82	0.65 ± 0.09	7
	iFLD	**0.87**	**0.12 ± 0.15**	7
CKA-2022 (350 m)	SFM	0.58*	**0.39 ± 0.13**	6
	SFMNN	**0.70***	**0.35 ± 0.17**	6
	iFLD	−0.87*	1.12 ± 0.21	4

Table 7
Performance metrics for different 3 different FLOX devices. We denote the different devices by the crop type the devices were pointed at. Metric definitions as in Table 6. Correlation scores r marked with * have $p > 0.05$. Mean absolute errors (MAE) are given in mW nm^{-1} sr^{-1} m^{-2}. We highlight the best results in bold font. N denotes the number of validation points.

Data		FLOX	r	MAE	N
CKA-2020 (350 m)	SFM	Wheat (1)	**0.62**	0.48 ± 0.05	11
		Wheat (2)	0.86	**0.30 ± 0.07**	14
		Oat	**0.84**	0.33 ± 0.06	12
		All	**0.90**	0.36 ± 0.04	37
	SFMNN	Wheat (1)	0.59*	**0.31 ± 0.06**	11
		Wheat (2)	**0.90**	0.49 ± 0.09	14
		Oat	0.39*	**0.23 ± 0.07**	12
		All	0.86	0.35 ± 0.04	37
	iFLD	Wheat (1)	−0.19*	**0.33 ± 0.07**	11
		Wheat (2)	0.11*	**0.34 ± 0.09**	13
		Oat	0.10*	**0.17 ± 0.09**	12
		All	0.55	**0.28 ± 0.05**	36
CKA-2020 (600 m)	SFM	Wheat (1)	**0.88***	0.85 ± 0.09	4
		Wheat (2)	0.86	**0.32 ± 0.10**	10
		Oat	0.69	0.34 ± 0.06	9
		All	**0.83**	0.42 ± 0.05	23
	SFMNN	Wheat (1)	0.81*	**0.11 ± 0.08**	4
		Wheat (2)	**0.90**	**0.31 ± 0.10**	10
		Oat	**0.73**	0.36 ± 0.06	9
		All	**0.83**	**0.29 ± 0.05**	23
	iFLD	Wheat (1)	−0.56*	0.51 ± 0.10	5
		Wheat (2)	0.24*	0.45 ± 0.16	9
		Oat	0.10*	**0.25 ± 0.10**	9
		All	0.52	0.39 ± 0.08	23

different FLOX measurement set-ups. It can be observed, however, that the best performing method in r and MAE also performs best on a majority of the individual FLOX set-ups such that the overall performance assessment in Table 6 is not driven by single set-ups in the CKA-2020 data sets. Furthermore, the variation of MAE across the different measurement set-ups is of the same order as the large uncertainties on the MAEs of individual measurement set-ups for all methods.

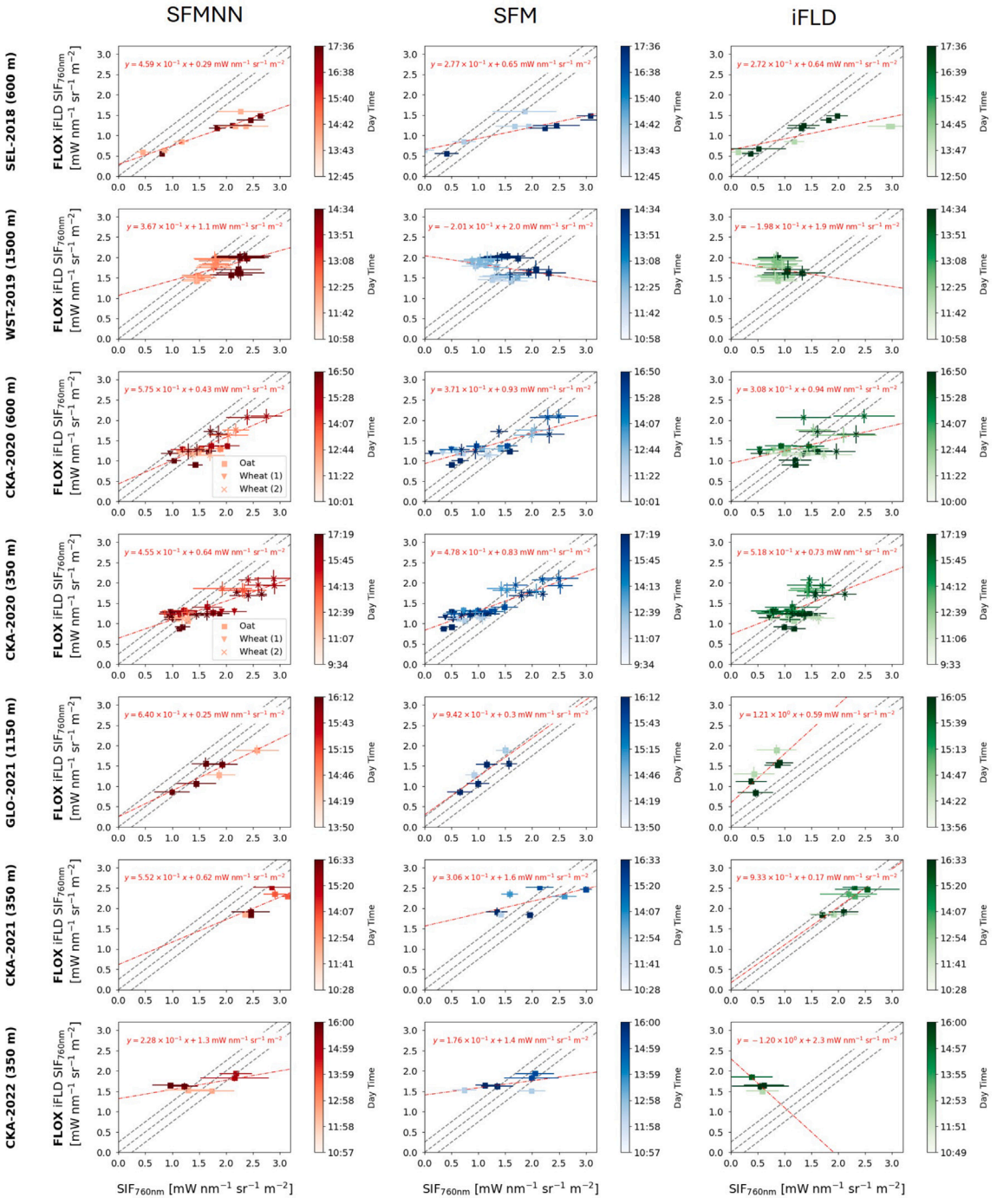

Fig. 8. FLOX derived iFLD SIF vs. HyPlant derived SFMNN, SFM and iFLD SIF in the 7 in-situ validation data sets (see Table 1). (For interpretation of the references to color in this figure legend, the reader is referred to the web version of this article.)

As a conclusion, we highlight that the SFMNN performs best in terms of r but is impacted by prediction bias. In particular, SFMNN showed sensitivity to in-situ FLOX SIF data sets where both iFLD and SFM do not (WST-2019, CKA-2022). Strong positive bias in all datasets leads to an underperformance of SFMNN with respect to iFLD and SFM in various data sets such that it only outperforms these two baseline methods in less than half of the considered validation data sets. Furthermore, a restricted comparison of the performance of individual and aggregated FLOX performance metrics in the CKA-2020 datasets indicates that iFLD, SFM and SFMNN performances can be generalized across the different measurement set-ups within single campaigns given the large uncertainties associated of both the FLOX and the HyPlant SIF estimates.

4.3. Application study 1: Retrieval of SIF in the diurnal course

In this application study we analyze the diurnal course of SFMNN predicted SIF and assess whether it peaks around the solar noon or if, contrarily, the largest fluorescence values can be found prior to or after solar noon. We formulate this plausibility test on the diurnal data set D_{day}, by investigating the overall diurnal course of predicted SIF over a large number of pixels. The SIF predictions for the nine HyPlant acquisitions in D_{day} were georegistered to form time series $f(\underline{x}, t)$ in each georegistered pixel $\underline{x}$ (see Fig. 10). We detrended each

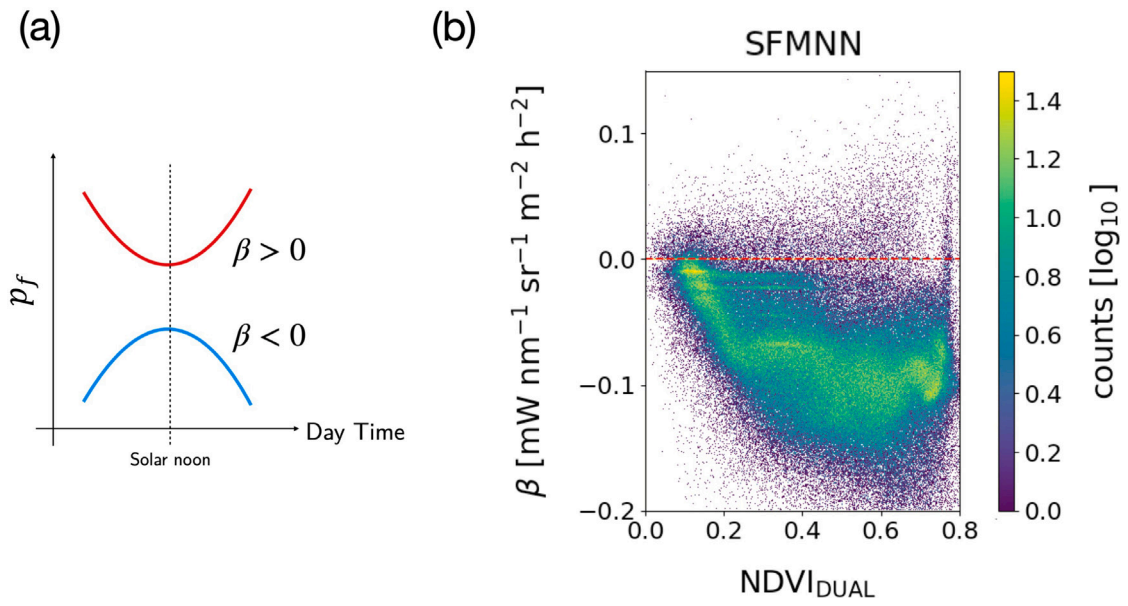

Fig. 9. (a) Sketch of two possible time series of predicted fluorescence $f(\underline{x}, t)$. Only the blue time series with $\beta < 0$ is considered plausible as it peaks during solar noon. (b) Histogram of SFMNN β-NDVI relationship shown in Fig. 10. (For interpretation of the references to color in this figure legend, the reader is referred to the web version of this article.)

time series independently and fitted a second order polynomial $p_f(\underline{x})$ to the time series in each pixel. The second order derivative of this polynomial with respect to time $\partial^2 p_f / \partial t^2 = \beta$ then was used as a proxy for the diurnal SIF dynamics (see Fig. 9(a)). In particular, we indicate whether the predicted SIF peaks around solar noon ($\beta < 0$) or in morning and evening ($\beta \geq 0$) acquisitions. In physiologically plausible SIF time series of healthy vegetation under a typical course of diurnal solar irradiance variation without shadowing, we expect $\beta < 0$ over the whole NDVI domain. The map of β for $\mathcal{D}_{\text{day}}$ in Fig. 10 highlights that pixels with $\beta > 0$ are mainly distributed parallel to tree lines where the strong shadowing in the diurnal course invalidates the model assumptions. SFMNN predictions thus yield a plausible diurnal course of SIF.

4.4. Application study 2: Retrieval of SIF in hilly terrain

In this application study we show that the constraints imposed on SFMNN's weight optimization yield topography-aware predictors. To this end, we have trained SFMNN p^t_{600}, p^t_{1150}, p^t_{1500} and p^t_{1800} on the data sets $\mathcal{D}^t_{600}$, $\mathcal{D}^t_{1150}$, $\mathcal{D}^t_{1500}$ and $\mathcal{D}^t_{1800}$ exhibiting large topographic variation. For this we compare the geometrical path length d to the fractional band depth

$$n_{O_2A} = \frac{t_{\text{tot}}(760.5\,\text{nm})}{t_{\text{tot}}(755\,\text{nm})} \tag{21}$$

predicted by SFMNN for each spatial pixel. The path length is defined as the distance computed from the surface to the sensor considering the flight height, topography and the instantaneous viewing angle at recording time.

In Fig. 11 we show an exemplary acquisition of a strong topographic gradient along a height difference of ~140 m. The SFMNN predictor adapts the predicted band depth locally to gain a similar $\text{nMAE}_{\mathcal{W}_{O_2A}}$ over the full topographic change (see Figs. 11 and 12(a)). As a result we can observe a relatively constant SFMNN SIF prediction along-track for the different height ranges (see Figs. 11 and 12(b)). A small increase of maximum SIF can still be observed over the topographic change (and d decrease). It is, however, not possible to completely disassociate this SIF distribution shift from a possible change in surface conditions. This is also visible in Fig. 12(b) where we show the SIF prediction distribution as a function of the topography. Similarly, the distribution of spectral wavelength shifts $\Delta\lambda_{x,y}$ and ρ_{752} are approximately constant in the along track dimension, suggesting that the model does not compensate the atmospheric transfer over the hill slope by varying these parameters.

The predicted O_2-A band depth is not completely decoupled from surface related quantities. This can be seen in the exemplary acquisition plot in Fig. 11 in some correlated features in SIF in n_{O_2A}. We cannot determine from observational data whether this coupling is physical (i.e. conditioned by common causal factors) or conditioned by a learned empirical distribution. Furthermore, there is an unphysical artefact visible in the band depth estimation that correlates with a region of high reconstruction errors $\text{nMAE}_{\mathcal{W}_{O_2A}}$ (see Fig. 11). While we cannot pinpoint exactly, what the reason for this prediction failure is, we test for consistency of n_{O_2A} in general prediction scenarios. In order to assess whether the variation in predicted band depth n_{O_2A} is consistent across multiple acquisitions and across different predictors, in Fig. 13 we show the linear extinction factor $s_{n_{O_2A}}$ defined as the first-order derivative to the approximation

$$\mathbb{E}\left[n_{O_2A} \mid d\right] = s_{n_{O_2A}} \cdot d + \text{const.} \tag{22}$$

where d denotes the geometric path between the surface and sensor. As we are interested in the sensitivity of n_{O_2A} to the changing geometric path length, we summarize any other influencing factor under *const.* and determine $s_{n_{O_2A}}$ with a linear fit to the conditional distribution $p(n_{O_2A}|d)$ as shown in Fig. 12(a). We find that $s_{n_{O_2A}}$ stabilizes at a constant value in acquisitions with large differences in geometric path lengths $\Delta d = \max d - \min d$. This is true for acquisitions of different SFMNN models and across different data sets. As expected, the variation in the $s_{n_{O_2A}}$ estimates increases when the geometric path length differences Δd become smaller and the uncertainty on the per-acquisition expectation $\mathbb{E}\left[n_{O_2-A} \mid d\right]$ increases. As a consequence, the effect of variable d cannot be ascertained in acquisitions with small Δd. The smaller predicted band depth differences are more strongly driven by other, possibly non-physical factors. However, in acquisitions with larger Δd band depth changes are explained by a common atmospheric transfer model yielding a constant $s_{n_{O_2A}}$ (Fig. 13). This common transfer model is predicted by independent SFMNN models. We find thus a strong indication that SFMNN models converge to solutions where topographic changes are explained mainly by changing atmospheric

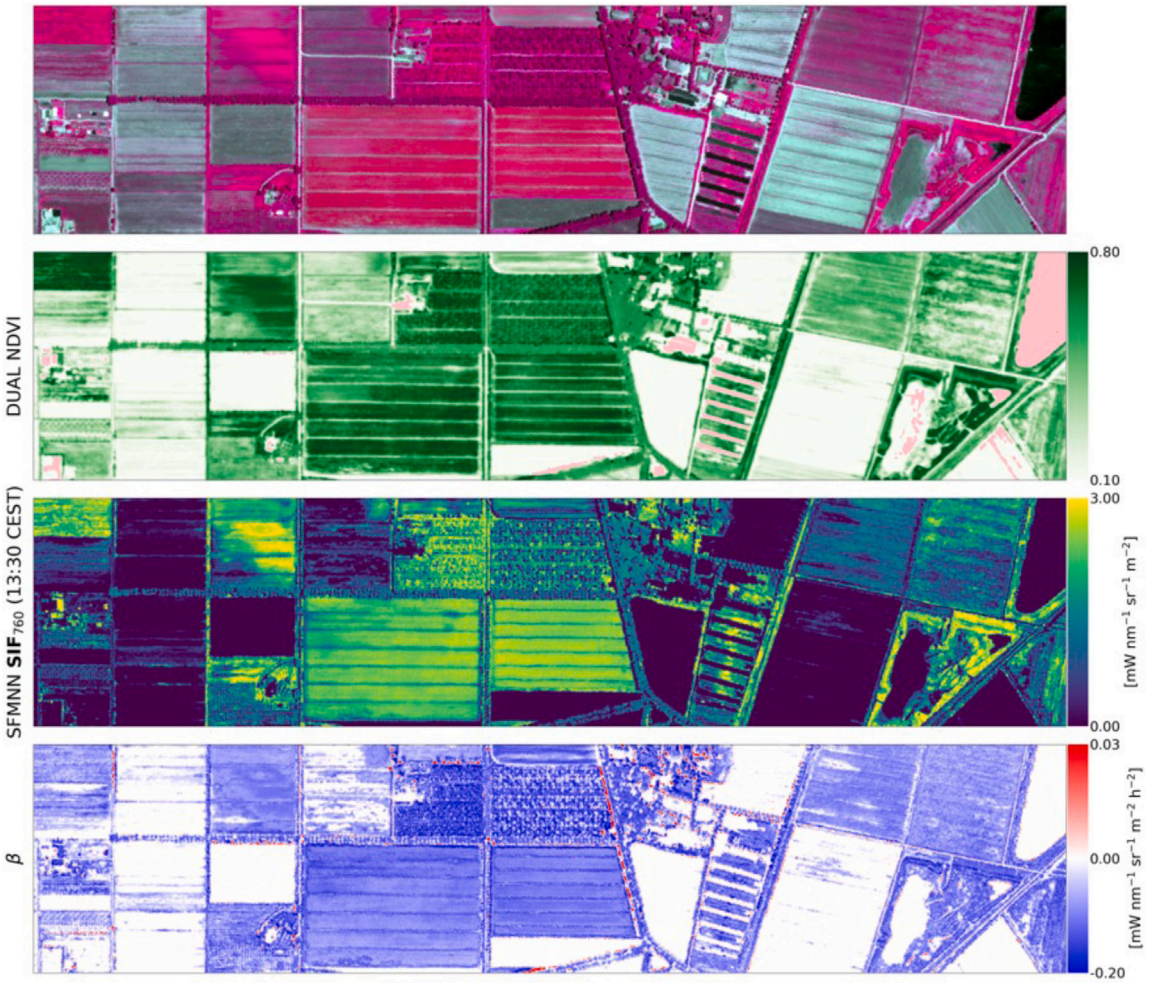

Fig. 10. We show a pseudo-color image (FLUO NIR, red and green) of the WST-2019 (1500 m) 13:30 CEST acquisition (first row), the corresponding NDVI computed from DUAL (second row), the SFMNN SIF prediction (third row) and the diurnal SFMNN SIF variation parameterized by β (fourth row). Pixels with invalid NDVI values (in shaded, barren and water pixels) are highlighted in pink. (For interpretation of the references to color in this figure legend, the reader is referred to the web version of this article.)

transfer and not, for example, by increasing fluorescence.

5. Discussion

5.1. Reconstruction performance

Since the SFM is the operational spectral fitting SIF retrieval algorithm for HyPlant data, its prediction as well as reconstruction performance has been repeatedly validated using top-of-canopy spectral measurements (Rascher et al., 2021; Cogliati et al., 2019; Siegmann et al., 2021) and cross-validated with SIF products from different platforms (Wang et al., 2022). Matching SFM's reconstruction performance is thus an important feature of novel spectral fitting algorithms aiming to retrieve SIF in addition to a good performance against other baseline methods applied to HyPlant data such as iFLD. While a good reconstruction performance does not validate the physicality of our approach, it constitutes a necessary precondition for any spectral fitting method. Failure to satisfactorily approximate the model to observations could indicate either an incomplete model formulation or too stringent constraints imposed as regularization on the fitting process.

We could show that the reconstruction performance of SFMNN is comparable to SFM in a data set of nine HyPlant acquisitions recorded over the course of a single day. SFMNN's reconstruction led to smaller MAE than SFM inside and to only slightly worse performance outside of the O_2-A absorption band. We hypothesize that the SNR-based loss weighting, which increases the importance of residuals within the absorption band, led to this preferential improvement of absolute residuals as no such prior assumption is considered in the spectral fitting process of SFM. In parallel, the improved reconstruction performance of SFMNN could be observed when analyzing its radiance normalized residuals nMAE inside the O_2-A band. We found the same differentiation in nMAE between *noon* and *off-noon* conditions for SFMNN as for SFM. Worse nMAE are found in *off-noon* conditions. This performance deterioration could also be established in SFMNN residual statistics of multiple acquisitions (cf. Fig. 6).

We have investigated the cause for this decreased reconstruction performance and find that it is likely due to lacking disentanglement of reflectance and atmospheric transfer performance in *off-noon* conditions. In Fig. 14 we show that SFMNN's reflectance prediction is not accurate in *off-noon* conditions. A significant underestimation of SFMNN as compared to georegistered DUAL reflectances can be observed in the morning and afternoon while the *noon* acquisitions show comparable reflectance distributions. In order to reduce the reconstruction error the network predictor instead increases the diffuse contributions to the at-sensor radiance in *off-noon* predictions as can be seen in Fig. 15, where we show the mean nadir t_{tot} in all D_{day} (a) and the simulated t_{tot} in black (b). The simulation is performed by (i) simulating L^{at-s} using a MODTRAN derived radiative transfer emulator Pato et al., 2024) and (ii) normalizing with the solar irradiance and reflectance model used in this work. We parameterize the simulation of

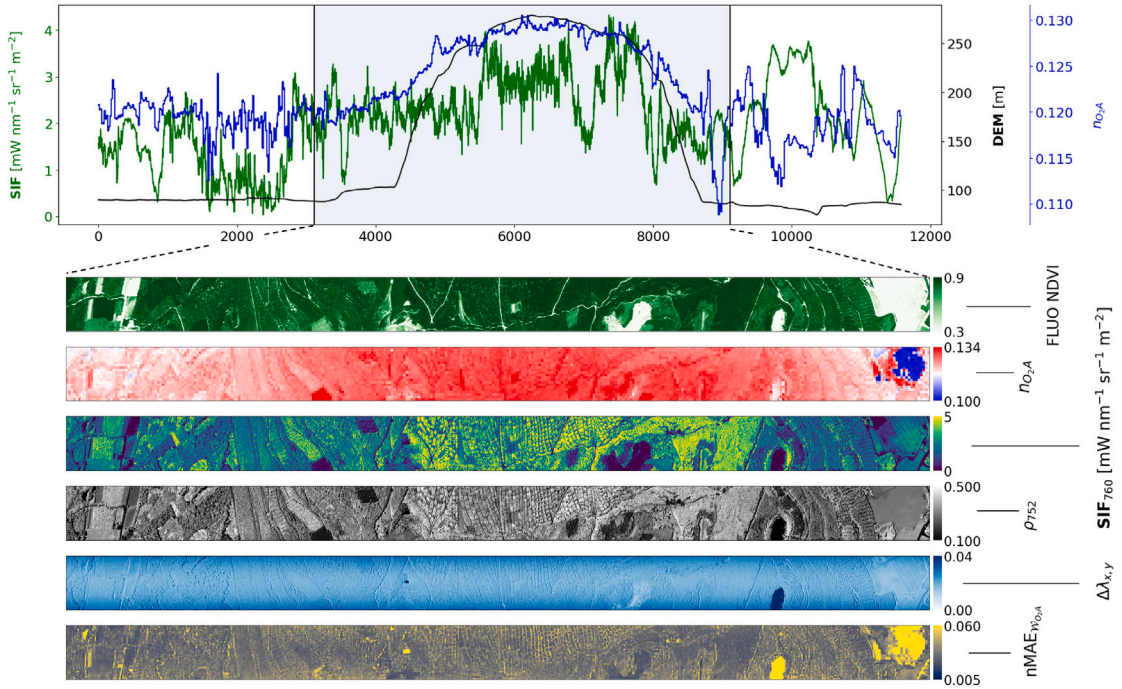

Fig. 11. An exemplary airborne data acquisition with pronounced topographic variation (SOP-2023, 2023/06/23 14:44 CEST). In the first row we show SFMNN SIF prediction (green), a digital elevation map (DEM) of the scene (black) and the predicted n_{O_2A} (blue) averaged over the across-track dimension. In the second to fourth row we show maps of FLUO derived NDVI, n_{O_2A}, SFMNN SIF SFMNN predicted reflectance at 740 nm, SFMNN predicted wavelength shifts $\Delta\lambda_{x,y}$ and reconstruction errors nMAE$_{\mathcal{W}_{O_2A}}$. (For interpretation of the references to color in this figure legend, the reader is referred to the web version of this article.)

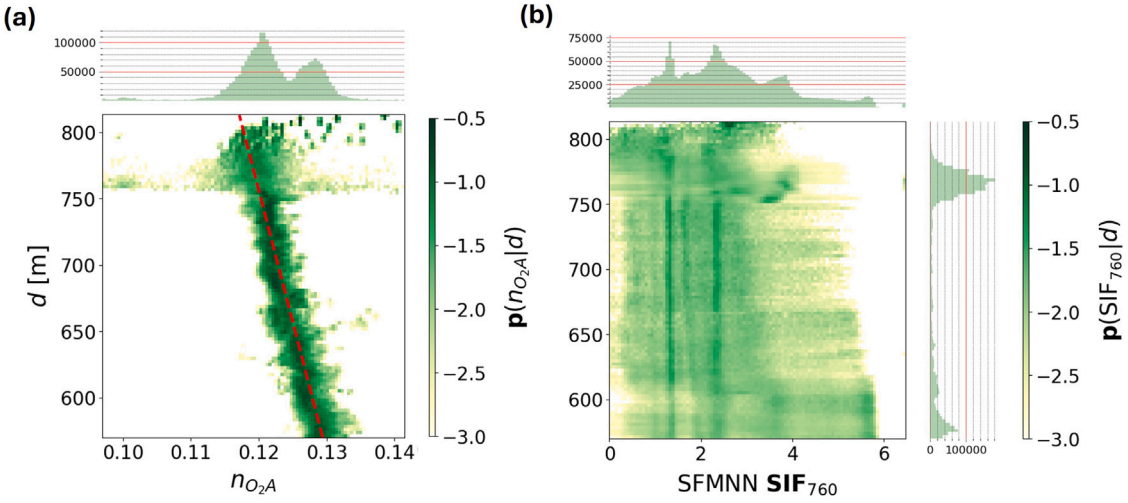

Fig. 12. **(a)**: Distribution $p(n_{O_2A}|d)$ (O_2-A band depth as a function of geometric path length d) (green) and linear fit (red) of the acquisition shown in Fig. 11 (SOP-2023, 2023/06/23 14:44 CEST). **(b)**: Distribution $p(\mathrm{SIF}_{760}|d)$ (SFMNN SIF as a function of geometric path length d). (For interpretation of the references to color in this figure legend, the reader is referred to the web version of this article.)

L_{HyP} with the mean values assumed for D_{day} *noon* acquisitions. We also show simulations under shifts $\Delta\rho$ and Δe which denote shifts between the parameter values for ρ and e used in the simulation of the at-sensor radiance and the parameter values used for normalization in Eq. (18). The simulation under a shift $\Delta\rho = 0.05$ can explain both the large variation between predicted t_{tot} in *noon* and *off-noon* the acquisitions. The shift and $\Delta e > 0$ furthermore explains the sloping behavior of the predicted transfer functions in all acquisitions (Fig. 15 (a)). Overall, this shows that SFMNN cannot fully disentangle the reflectance contribution from the atmospheric transfer. The regularization $\ell_{\mathbf{atm}}$ (Eq. (19)) proves to be insufficient in *off-noon* conditions. While we could not yet pinpoint the exact reasons for the difference in disentangling capacity of SFMNN in *noon* and *off-noon* conditions, we posit that there are three plausible reasons.

First, there is increasing model incompatibility under more diffuse conditions as could be seen in Fig. 5. The physical model used for signal reconstruction in Eq. (1) includes a diffuse contribution to the at-sensor signal, but the approximate PCA-based formulation of the atmospheric transfer lacks accuracy for the representation of τ_{do} and ρ_{so} which become more important under low SZA conditions.

Secondly, the worse performance may be due to data quality deterioration in lower light conditions. At lower SZA the diffuse contribution to the at-sensor radiance increases strongly even under clear-sky conditions when HyPlant data is normally recorded. An increasing diffuse component, however, reduces the signal-to-noise ratio of the at-sensor radiance as the pixelwise hyperspectral signal is spatially mixed.

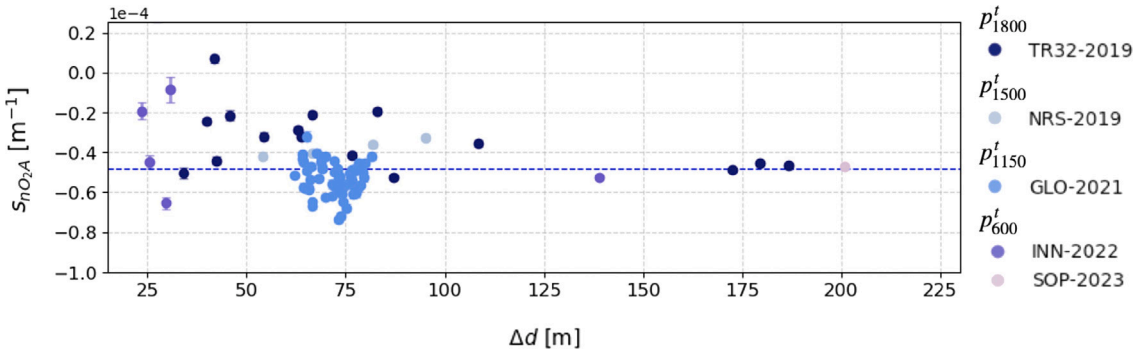

Fig. 13. Estimated $s_{n_{O_2A}}$ for all acquisitions with relevant variation in topography (cf. *topo* in Table 2). The dashed line represents the mean of five acquisitions with largest Δd. (For interpretation of the references to color in this figure legend, the reader is referred to the web version of this article.)

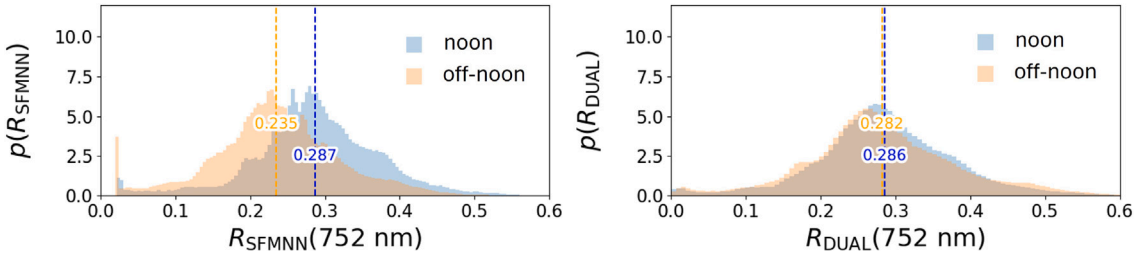

Fig. 14. Marginal reflectance distributions as predicted by SFMNN (a) and measured by DUAL (b) in the D_{day} data set. *Noon* and *off-noon* acquisition statistics are shown separately. (For interpretation of the references to color in this figure legend, the reader is referred to the web version of this article.)

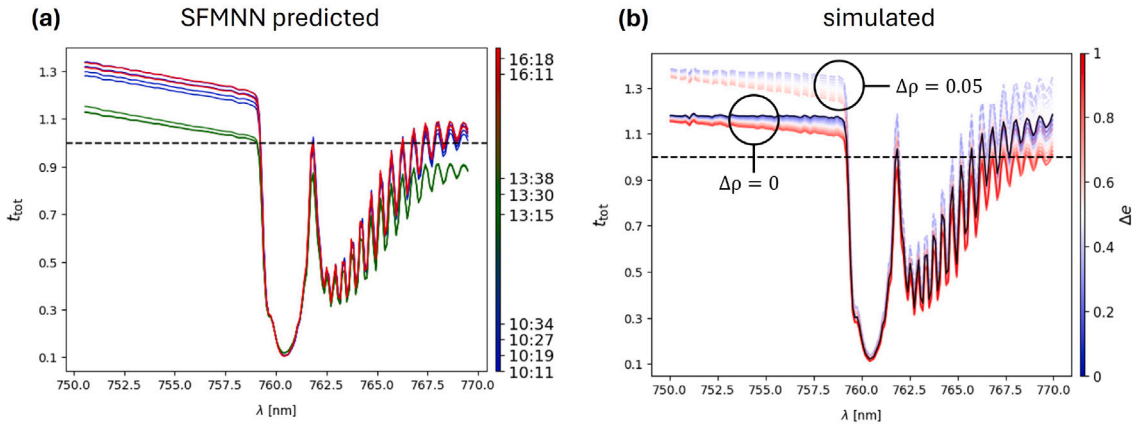

Fig. 15. **(a)** Mean SFMNN predicted atmospheric transfer t_{tot} in the nadir position in all acquisitions of D_{day}. **(b)** Simulated t_{tot} (black) simulation parameterization: AOT = 0.05, H_2O = 0.1, tilt angle TA = 0°, SZA = 30°, relative azimuth angle RAA = 30°, ground surface height h_{gnd} = 0.1 km, sensor height above ground h_{sen} = 1.6 km, ρ_{740} = 0.28, s_ρ = 0.007, e = 0. $\Delta\rho$ and Δe denote simulations where the normalizing reflectance in Eq. (18) was simulated with a shifted value with respect to the value used for at-sensor radiance calculation. (For interpretation of the references to color in this figure legend, the reader is referred to the web version of this article.)

The reduction in SNR is further enhanced due to the overall lower light intensity. This might reduce the ability of the network to disentangle reflectance and atmospheric components of the at-sensor signal.

Thirdly, the circumstance that the similitude of the predicted atmospheric transfer function with respect to our simulation in Fig. 15(b) is significantly improved under a change Δe indicates that the model does not represent surface reflectances accurately in the parameter space spanned by ρ, s_ρ and e (see Eq. (9)). This may in turn force the unphysical boosting of diffuse components.

The lack of control over the atmospheric decomposition is a significant draw-back of the PCA-based parameterization as compared to a physically based prediction of atmospheric components. This work

has only addressed the atmospheric at-sensor contribution in an aggregated way by analyzing the variation of the O_2-A band depth under topographic changes (Section 4.4) and the disentangling capacity of reflectance from atmospheric transfer in this section. Further work should therefore evaluate quantitatively the predicted atmospheric components and concentrate on proposing physical constraints regarding the disentangling of individual atmospheric components.

A promising possibility to constrain further the simulated atmospheric transfer consists in replacing the PCA-based forward simulation in SFMNN with a differentiable emulator of a physically accurate radiative transfer model. Research in biophysical modeling and simulation of hyperspectral reflectance from various platforms (Vicent et al., 2016; De Grave et al., 2020; Verrelst et al., 2021) are the basis for fast and accurate emulation models (Verrelst et al., 2016, 2017) and may be leveraged for computationally efficient retrieval of biophysical parameters. The emulation of at-sensor radiance simulations, as would be needed in our approach, has been addressed in Pato et al. (2024), Vicent et al. (2018). The differentiable nature of a number of those emulator models warrants an investigation into possibilities to implement such a replacement that would implement a tight integration of physically and statistically based SIF retrieval as has been shown recently for DESIS (Buffat et al., 2024a). Furthermore, the use of sensor-specific emulation facilitates the generalization of SFMNN to other airborne hyperspectral imaging sensors such as CFIS (Frankenberg et al., 2018), as well as to other spaceborne imaging sensors with appropriate spatial and spectral resolution such as FLEX (Drusch et al., 2017). With the use of emulators the radiative transfer physics and sensor characteristics affecting the at-sensor radiance can be modularized by domain experts and do not need to be modelled by the network as has been the case in this work where the atmospheric transfer was reconstructed from PCA weights on the fly. Such a procedure can exclude non-physical or implausible efficiently by imposing hard constraints on the at-sensor radiance model.

5.2. Accuracy of the SFMNN top-of-canopy SIF product

Direct validation with high-quality predictions from top-of-canopy measurements is the gold-standard for any SIF retrieval scheme if the spatial resolution of the sensor data is high enough to resolve the measurement footprint of the top-of-canopy measurements. The acquisition of field data and its synchronization with sensor acquisitions is, however, costly and usually results in small and spatially very constrained validation data sets. In this work we have gathered the majority of FLOX derived top-of-canopy SIF estimates acquired in tandem with HyPlant flights covering the period 2018–2022 to thoroughly validate SFMNN with high-quality data (see Table 6). While this study is the largest and most complete systematic comparison of HyPlant derived SIF estimates with top-of-canopy FLOX measurements, the validation data set has still a limited size and mainly covers crop canopies. Moreover, in addition to the uncertainties on the geolocalization and time synchronization, that were considered in this work, other uncertainty sources can impact the comparison of HyPlant derived SIF and FLOX derived SIF. Most importantly, we could not quantify uncertainties related to different viewing angles of in-situ and airborne radiance measurements (Liu et al., 2016).

In our validation study we could show that SFMNN prediction resulted in a reduction of the absolute error with respect to SFM and an improvement of correlation scores r with respect to iFLD. With SFMNN we found the best correlation scores r overall. SFMNN, however, was shown to still be impacted by biases leading to overestimation of SIF in absolute terms that lead to a similar performance as iFLD in terms of MAE. iFLD, on the other hand, clearly underperformed in terms of r as compared to SFM and SFMNN.

We found SFMNN MAE covering the range from 0.2–0.7 mW nm^{-1} sr^{-1} m^{-2} depending on the campaign data set used for validation. The FLEX mission requirement for SIF retrieval accuracy of 0.2 mW nm^{-1} sr^{-1} m^{-2} (Vicent et al., 2016) could not be consistently achieved for HyPlant data with the current set-up using one of the three SIF retrieval methods (iFLD, SFM, SFMNN) that were investigated in this study.

5.3. Learning of implicit constraints

We have shown in two application studies that SFMNN predictions are constrained implicitly. The observation of a constraint on the second order derivative β in diurnal SIF products suggests that the network is able to learn a first order physiological relationship between day time (i.e. SZA) and SIF emission magnitude. On the other hand, it could be shown that the atmospheric transfer function could be adapted in a way to represent the variation of the optical path in acquisitions solely based on radiance data. The fact that the feature based internal representations learned by SFMNN can be shown to be sensitive to basic physiological and physical constraints emphasizes that the proposed loss formulation allows the network to generalize the disentangling in typical HyPlant recording conditions beyond a pure functional optimization as it is done in SFM. This aspect of SFMNN can be considered to be an important advantage of SFMNN over the methodologies followed by SFM and iFLD as it allows in principle the use of trained models on data that was not included in the training. If a single model could be applied directly to new data prediction times could be significantly reduced as compared to the approach followed here (pretraining and fine-tuning) as well as compared to related spectral fitting methods such as SFM. Further validation should therefore especially concentrate on the generalization capacity of SFMNN SIF prediction for an operational context where fast prediction times are advantageous.

The feature representation of the hyperspectral signal as learned by the SFMNN encoder is based on a restricted number of HyPlant acquisitions. Recent scientific breakthroughs in the domain of neural network training for vision applications draw however on the self-supervised, application-agnostic learning of feature representations from very large data sets. Recently, first adaptations of large Vision Transformer and Diffusion models have been developed for remote sensing RGB (Wang et al., 2023; Khanna et al., 2023) and multispectral imagery (Blumenstiel et al., 2024). The multitude of spaceborne, globally distributed hyperspectral datasets that have become and will be available in the near future (PRISMA Pignatti et al., 2013, EnMAP Guanter et al., 2015b, DESIS Krutz et al., 2019, FLEX Drusch et al., 2017, CHIME Celesti et al., 2022) are likely to allow similar training set-ups. A natural extension of the present work will therefore consist in adapting the training of the SFMNN encoder backbone to a large collection of hyperspectral data sets from different sensors and platforms to improve its representative power.

6. Conclusion

We have presented in this work SFMNN, a self-supervised deep learning method to estimate SIF in the O_2-A absorption band of hyperspectral HyPlant imagery. We have applied the method to HyPlant acquisitions from multiple years and different observational conditions and compared the results to both an SFM and an iFLD SIF retrieval method for HyPlant data by performing a validation with ground based FLOX measurements. This is the first time that HyPlant SIF retrieval methods and products have been compared systematically in a validation with a FLOX in-situ data set spanning multiple years. In this validation study with in-situ measured SIF in flat terrain we could show that SFMNN yielded state-of-the-art SIF predictions in terms of its correlation score outperforming both iFLD and SFM. In terms of accuracy we found that SFMNN is impacted by an overestimating bias. Despite this bias SFMNN outperformed SFM in terms of accuracy.

In a second study on predicted diurnal SIF variation we found that the expected diurnal SIF dynamics in vegetated and non-vegetated areas were physiologically plausible. We have shown that SFMNN could

learn implicitly a first order physiological constraint regarding day time (i.e. SZA) and SIF emission magnitude.

We could furthermore observe that SFMNN could be applied to HyPlant data taken in regions with large topographic variation. One of the most serious issues of the baselines considered in this work is to find a suitable parameterization of the atmospheric transfer in regions with changing atmospheric and observational conditions. As SFMNN can locally compensate such changes in principle, an increased interest was put in its ability to yield trustworthy SIF estimates in such conditions. Since no in-situ data was available for flight lines exhibiting large topographic changes, we could only conduct a qualitative analysis. We found that the effective extinction coefficient determined from the linear relationship between O_2-A band depth and the estimated radiative path length converged to a constant value in flight lines with large topographic variations.

CRediT authorship contribution statement

Jim Buffat: Writing – review & editing, Writing – original draft, Visualization, Validation, Software, Methodology, Investigation, Formal analysis, Data curation, Conceptualization. **Miguel Pato:** Writing – review & editing, Supervision, Project administration, Funding acquisition, Conceptualization. **Kevin Alonso:** Writing – review & editing, Conceptualization. **Stefan Auer:** Writing – review & editing, Project administration, Funding acquisition, Conceptualization. **Emiliano Carmona:** Writing – review & editing, Conceptualization. **Stefan Maier:** Writing – review & editing, Conceptualization. **Rupert Müller:** Conceptualization. **Patrick Rademske:** Data curation. **Bastian Siegmann:** Writing – review & editing, Data curation. **Uwe Rascher:** Writing – review & editing, Supervision, Project administration, Funding acquisition, Data curation, Conceptualization. **Hanno Scharr:** Writing – review & editing, Supervision, Project administration, Methodology, Funding acquisition, Conceptualization.

Declaration of competing interest

The authors declare the following financial interests/personal relationships which may be considered as potential competing interests: Jim Buffat reports financial support was provided by Helmholtz Artificial Intelligence Cooperation Unit. Miguel Pato reports financial support was provided by Helmholtz Artificial Intelligence Cooperation Unit. Kevin Alonso reports financial support was provided by Helmholtz Artificial Intelligence Cooperation Unit. Stefan Auer reports financial support was provided by Helmholtz Artificial Intelligence Cooperation Unit. Emiliano Carmona reports financial support was provided by Helmholtz Artificial Intelligence Cooperation Unit. Rupert Mueller reports financial support was provided by Helmholtz Artificial Intelligence Cooperation Unit. If there are other authors, they declare that they have no known competing financial interests or personal relationships that could have appeared to influence the work reported in this paper.

Acknowledgments

This work is part of the project “FluoMap” (Impulsfonds-Förderkennzeichen ZT-I-PF-5-12) funded by the Helmholtz Initiative and Networking Fund, Helmholtz AI, Deutsches Zentrum für Luft- und Raumfahrt (DLR) and Forschungszentrum Jülich GmbH (FZJ). The authors gratefully acknowledge computing time on the supercomputer JURECA (Jülich Supercomputing Centre, 2021) at Forschungszentrum Jülich under grant no. fluomap-ct. We gratefully acknowledge the financial support by the European Space Agency (ESA) for airborne data acquisition and data analysis in the frame of the FLEXSense campaign (ESA Contract No. 4000125402/ 18/NL/NA) and the Phototproxy project (ESA contract No. 4000125731/19/NL/LF). Additionally, HyPlant and FLOX data acquisition has partially been funded by the German Federal Ministry of Education and Research within the German-Plant-Phenotyping Network (DPPN) (project identification number: 031A053), the ‘Strukturwandel-Projekt Bioökonomie REVIER’, which is funded by the German Federal Ministry of Education and Research (project identification number 031B0918A), the Deutsche Forschungsgemeinschaft (DFG, German Research Foundation) under Germany’s Excellence Strategy – EXC 2070–390732324 and the project Land surface Interactions with the Atmosphere over the Iberian Semi-arid Environment (LIAISE) funded by the Centre national de la recherche scientifique (CNRS). Open access is funded by the Deutsche Forschungsgemeinschaft (DFG, German Research Foundation) – 491111487.

Appendix. Derivation of SNR-based loss weighting

Let us consider a simplified model for SIF estimation and assume we have N measurements y on two wavelengths λ_1 and λ_2. Signal is composed by a reflectance part $y_R(\lambda)$ and a fluorescence part $y_R(\lambda)$ including atmospheric influences, such that

$$y(\lambda) = y_R(\lambda) + y_f(\lambda) + \epsilon, \tag{A.1}$$

where ϵ denotes represents instrumental noise. We model $R(\lambda)$ and $f(\lambda)$ to be

$$R(\lambda_i) = c_R(\lambda_i) R_0 \tag{A.2}$$

$$f(\lambda_i) = c_f(\lambda_i) f_0 \tag{A.3}$$

with known, constant function $c_\cdot(\lambda)$ and scalar parameters R_0 and f_0. In a more realistic model there would be more than one parameter for R and f. Please note, that we can select $c_\cdot(\lambda)$ such that $\mathbb{E}[R_0] = 1$ and $\mathbb{E}[f_0] = 1$ if we want to. Our model equations for estimation are then

$$y(\lambda_1)_j = A_R(\lambda_1) c_R(\lambda_1) R_0 + A_f(\lambda_1) c_f(\lambda_1) f_0 + \epsilon_j \tag{A.4}$$

$$y(\lambda_2)_j = A_R(\lambda_2) c_R(\lambda_2) R_0 + A_f(\lambda_2) c_f(\lambda_2) f_0 + \epsilon_j \tag{A.5}$$

where A_R and A_f contain all atmospheric parameters and all the rest. Note, that the multiple measurements indicated by index j only change ϵ_j. Obviously, we can multiply each equation with a freely adaptable weight w_i without changing anything. We can rewrite the equation to be

$$\mathbf{W}\mathbf{y} = \mathbf{W}\mathbf{X}\boldsymbol{\beta} + \mathbf{W}\boldsymbol{\epsilon} \tag{A.6}$$

where $\mathbf{W}$ is a diagonal weight matrix with $W_{ii} = w_i$, $X_{i1} = A_R(\lambda_i) c_R(\lambda_i)$, $X_{i2} = A_f(\lambda_i) c_f(\lambda_i)$, $\beta_1 = R_0$, and $\beta_2 = f_0$. Noise ϵ has $\mathbb{E}(\epsilon|\mathbf{X}) = 0$ and $\mathrm{cov}(\epsilon|\mathbf{X}) = \boldsymbol{\Omega}$. In our case we assume that noise is independent, such that $\boldsymbol{\Omega}$ is diagonal with $\Omega_{ii} = w_i^2 u_i^2$, where u_i is the noise standard deviation for wavelength i. Clearly, weights w_i also scale the noise in the weighted equations. We know from Gauss–Markov-Theorem that the generalized least-squares estimator can then be written as

$$\hat{\boldsymbol{\beta}} = (\mathbf{X}^T \boldsymbol{\Omega}^{-1} \mathbf{X})^{-1} \mathbf{X}^T \boldsymbol{\Omega}^{-1} \mathbf{y} \tag{A.7}$$

where weights w_i cancel out. Using this simultaneous estimation of all parameters β_i for designing a suitable loss function is not obvious. We therefore investigate a special case, where only one parameter is unknown.

Let us assume R_0 to be known and we want to infer f_0. We can then reformulate (A.4) as

$$\tilde{\mathbf{y}} = \mathbf{X} f_0 + \boldsymbol{\epsilon} \tag{A.8}$$

where $\tilde{y}_i = y_i - y_{R,i}$ and $X_i = A_f(\lambda_i) c_f(\lambda_i)$. The BLUE is given by

$$\hat{f}_0 = \frac{\sum_i X_i \tilde{y}_i / u_i^2}{\sum_i X_i^2 / u_i^2} \tag{A.9}$$

or, more suggestively written

$$\hat{f}_0 = \sum_i \frac{1}{u_i^2} \frac{X_i}{\sum_j X_j^2 / u_j^2} \tilde{y}_i \tag{A.10}$$

For the usual Moore–Penrose pseudo-inverse we would get

$$\hat{f}_0 = \sum_i \frac{X_i}{\sum_j X_j^2} \tilde{y}_i \tag{A.11}$$

The difference between these two estimation approaches is in the weights

$$w_i = \frac{1}{u_i^2} \frac{\sum_j X_j^2}{\sum_j X_j^2 / u_j^2} \tag{A.12}$$

For training, we derive a mean weighting function $w_f = \mathbb{E}_p[w_i(L_{\text{at-s}}, f)]$ over a specific distribution p of simulated at-sensor radiances $L_{\text{at-s}}$ and top-of-canopy fluorescence. The simulations are performed in this case with a simple two-stream model, a fixed atmospheric transfer function and varying reflectance and fluorescence functions. Given the HyPlant-specific sensor variance model σ^2, this expectation can be written as

$$w_f(\lambda) = \left\langle \frac{1}{u_\lambda^2} \frac{\sum_{\lambda'} f_{\lambda'}^2}{\sum_{\lambda'} f_{\lambda'}^2 / u_{\lambda'}^2} \right\rangle_{p(L_{\text{at-s}}, f)} . \tag{A.13}$$

Data availability

The training and validation data will be made available. The DOI will be provided at a later stage of the review process.

References

Alonso, L., Gomez-Chova, L., Vila-Frances, J., Amoros-Lopez, J., Guanter, L., Calpe, J., Moreno, J., 2008. Improved fraunhofer line discrimination method for vegetation fluorescence quantification. IEEE Geosci. Remote. Sens. Lett. 5 (4), 620–624. http://dx.doi.org/10.1109/LGRS.2008.2001180.

Anderson, T.L., Charlson, R.J., Winker, D.M., Ogren, J.A., Holmén, K., 2003. Mesoscale variations of tropospheric aerosols*. J. Atmos. Sci. 60 (1), 119–136. http://dx.doi.org/10.1175/1520-0469(2003)060<0119:MVOTA>2.0.CO;2.

Bandopadhyay, S., Rastogi, A., Juszczak, R., 2020. Review of top-of-canopy sun-induced fluorescence (SIF) studies from ground, UAV, airborne to spaceborne observations. Sensors 20 (4), 1144. http://dx.doi.org/10.3390/s20041144.

Bandopadhyay, S., Rastogi, A., Rascher, U., Rademske, P., Schickling, A., Cogliati, S., Julitta, T., Mac Arthur, A., Hueni, A., Tomelleri, E., Celesti, M., Burkart, A., Stróżecki, M., Sakowska, K., Gąbka, M., Rosadziński, S., Sojka, M., Iordache, M.-D., Reusen, I., Van Der Tol, C., Damm, A., Schuettemeyer, D., Juszczak, R., 2019. Hyplant-derived sun-induced fluorescence—A new opportunity to disentangle complex vegetation signals from diverse vegetation types. Remote Sens. 11 (14), 1691. http://dx.doi.org/10.3390/rs11141691.

Bendig, J., Chang, C.Y., Wang, N., Atherton, J., Malenovský, Z., Rascher, U., 2021. Measuring solar-induced fluorescence from unmanned aircraft systems for operational use in plant phenotyping and precision farming. In: 2021 IEEE International Geoscience and Remote Sensing Symposium IGARSS. pp. 1921–1924. http://dx.doi.org/10.1109/IGARSS47720.2021.9555157.

Blumenstiel, B., Moor, V., Kienzler, R., Brunschwiler, T., 2024. Multi-spectral remote sensing image retrieval using geospatial foundation models. http://dx.doi.org/10.48550/arXiv.2403.02059, arXiv:2403.02059.

Buffat, J., Pato, M., Alonso, K., Auer, S., Carmona, E., Maier, S., Müller, R., Rademske, P., Rascher, U., Scharr, H., 2023. Deep learning based prediction of sun-induced fluorescence from hyplant imagery. In: IGARSS 2023 - 2023 IEEE International Geoscience and Remote Sensing Symposium. IEEE, Pasadena, CA, USA, pp. 2993–2996. http://dx.doi.org/10.1109/IGARSS52108.2023.10282828.

Buffat, J., Pato, M., Alonso, K., Auer, S., Carmona, E., Maier, S., Müller, R., Rademske, P., Rascher, U., Scharr, H., 2024a. Retrieval of sun-induced plant fluorescence in the o_2-A absorption band from DESIS imagery. arXiv:2411.08925, URL https://arxiv.org/abs/2411.08925.

Buffat, J., Rascher, U., Rademske, P., Siegmann, B., Junker-Frohn, L.V., Emin, D., 2024b. Hydata: HyPlant FLUO at-sensor radiance data packages and FLOX measurements for SIF retrieval method development from selected campaigns of the years 2018 - 2023. http://dx.doi.org/10.26165/JUELICH-DATA/QKJKPW.

Celesti, M., Rast, M., Adams, J., Boccia, V., Gascon, F., Isola, C., Nieke, J., 2022. The copernicus hyperspectral imaging mission for the environment (chime): status and planning. In: IGARSS 2022 - 2022 IEEE International Geoscience and Remote Sensing Symposium. pp. 5011–5014. http://dx.doi.org/10.1109/IGARSS46834.2022.9883592.

Chang, C.Y., Guanter, L., Frankenberg, C., Köhler, P., Gu, L., Magney, T.S., Grossmann, K., Sun, Y., 2020. Systematic assessment of retrieval methods for canopy far-red solar-induced chlorophyll fluorescence using high-frequency automated field spectroscopy. J. Geophys. Res.: Biogeosci. 125 (7), http://dx.doi.org/10.1029/2019JG005533, e2019JG005533.

Chang, C.Y., Wen, J., Han, J., Kira, O., LeVonne, J., Melkonian, J., Riha, S.J., Skovira, J., Ng, S., Gu, L., Wood, J.D., Näthe, P., Sun, Y., 2021. Unpacking the drivers of diurnal dynamics of sun-induced chlorophyll fluorescence (SIF): canopy structure, plant physiology, instrument configuration and retrieval methods. Remote Sens. Environ. 265, 112672. http://dx.doi.org/10.1016/j.rse.2021.112672.

Chen, X., Huang, Y., Nie, C., Zhang, S., Wang, G., Chen, S., Chen, Z., 2022. A long-term reconstructed TROPOMI solar-induced fluorescence dataset using machine learning algorithms. Sci. Data 9 (1), 427. http://dx.doi.org/10.1038/s41597-022-01520-1.

Cheng, Y.-B., Middleton, E.M., Zhang, Q., Huemmrich, K.F., Campbell, P.K.E., Corp, L.A., Cook, B.D., Kustas, W.P., Daughtry, C.S., 2013. Integrating solar induced fluorescence and the photochemical reflectance index for estimating gross primary production in a cornfield. Remote Sens. 5 (12), 6857–6879. http://dx.doi.org/10.3390/rs5126857.

Cogliati, S., Celesti, M., Cesana, I., Miglietta, F., Genesio, L., Julitta, T., Schuettemeyer, D., Drusch, M., Rascher, U., Jurado, P., Colombo, R., 2019. A spectral fitting algorithm to retrieve the fluorescence spectrum from canopy radiance. Remote Sens. 11 (16), 1840. http://dx.doi.org/10.3390/rs11161840.

Cogliati, S., Colombo, R., Celesti, M., Tagliabue, G., Rascher, U., Schickling, A., Rademske, P., Alonso, L., Sabater, N., Schuettemeyer, D., Drusch, M., 2018. Red and far-red fluorescence emission retrieval from airborne high-resolution spectra collected by the hyplant-fluo sensor. In: IGARSS 2018 - 2018 IEEE International Geoscience and Remote Sensing Symposium. pp. 3935–3938. http://dx.doi.org/10.1109/IGARSS.2018.8517758.

Cogliati, S., Verhoef, W., Kraft, S., Sabater, N., Alonso, L., Vicent, J., Moreno, J., Drusch, M., Colombo, R., 2015b. Retrieval of sun-induced fluorescence using advanced spectral fitting methods. Remote Sens. Environ. 169, 344–357. http://dx.doi.org/10.1016/j.rse.2015.08.022.

Colombo, R., Celesti, M., Bianchi, R., Campbell, P.K., Cogliati, S., Cook, B.D., Corp, L.A., Damm, A., Domec, J.C., Guanter, L., Julitta, T., Middleton, E.M., Noormets, A., Panigada, C., Pinto, F., Rascher, U., Rossini, M., Schickling, A., 2018. Variability of sun-induced chlorophyll fluorescence according to stand age-related processes in a managed loblolly pine forest. Global Change Biol. http://dx.doi.org/10.1111/gcb.14097.

Damm, A., Cogliati, S., Colombo, R., Fritsche, L., Genangeli, A., Genesio, L., Hanus, J., Peressotti, A., Rademske, P., Rascher, U., Schuettemeyer, D., Siegmann, B., Sturm, J., Miglietta, F., 2022. Response times of remote sensing measured sun-induced chlorophyll fluorescence, surface temperature and vegetation indices to evolving soil water limitation in a crop canopy. Remote Sens. Environ. 273, 112957. http://dx.doi.org/10.1016/j.rse.2022.112957.

Damm, A., Guanter, L., Laurent, V.C.E., Schaepman, M.E., Schickling, A., Rascher, U., 2014. FLD-based retrieval of sun-induced chlorophyll fluorescence from medium spectral resolution airborne spectroscopy data. Remote Sens. Environ. 147, 256–266. http://dx.doi.org/10.1016/j.rse.2014.03.009.

Damm, A., Guanter, L., Paul-Limoges, E., van der Tol, C., Hueni, A., Buchmann, N., Eugster, W., Ammann, C., Schaepman, M.E., 2015. Far-red sun-induced chlorophyll fluorescence shows ecosystem-specific relationships to gross primary production: An assessment based on observational and modeling approaches. Remote Sens. Environ. 166, 91–105. http://dx.doi.org/10.1016/j.rse.2015.06.004.

Damm, A., Paul-Limoges, E., Kükenbrink, D., Bachofen, C., Morsdorf, F., 2020. Remote sensing of forest gas exchange: Considerations derived from a tomographic perspective. Global Change Biol. 26 (4), http://dx.doi.org/10.1111/gcb.15007.

De Grave, C., Verrelst, J., Morcillo-Pallarés, P., Pipia, L., Rivera-Caicedo, J.P., Amin, E., Belda, S., Moreno, J., 2020. Quantifying vegetation biophysical variables from the sentinel-3/FLEX tandem mission: Evaluation of the synergy of OLCI and FLORIS data sources. Remote Sens. Environ. 251, 112101. http://dx.doi.org/10.1016/j.rse.2020.112101.

Drusch, M., Moreno, J., Del Bello, U., Franco, R., Goulas, Y., Huth, A., Kraft, S., Middleton, E.M., Miglietta, F., Mohammed, G., Nedbal, L., Rascher, U., Schüttemeyer, D., Verhoef, W., 2017. The fluorescence explorer mission concept—ESA's earth explorer 8. IEEE Trans. Geosci. Remote Sens. 55 (3), 1273–1284. http://dx.doi.org/10.1109/TGRS.2016.2621820.

European Space Agency, 2017a. Technical assistance for the deployment of an advanced hyperspectral imaging sensor during FLEX-EU. http://dx.doi.org/10.5270/ESA-20835d4.

European Space Agency, 2017b. Technical assistance for the deployment of an advanced hyperspectral imaging sensor during soyflex. http://dx.doi.org/10.5270/ESA-50a3dd4.

European Space Agency, 2018. Technical assistance for the deployment of an advanced hyperspectral imaging sensor during SoyFLEX2. http://dx.doi.org/10.5270/ESA-24b3118.

European Space Agency, 2019. Photoproxy: technical assistance for the photosynthetic-proxy experiment. http://dx.doi.org/10.57780/esa-bb0ea39.

Frankenberg, C., Butz, A., Toon, G.C., 2011. Disentangling chlorophyll fluorescence from atmospheric scattering effects in O2 A-band spectra of reflected sun-light. Geophys. Res. Lett. 38 (3), http://dx.doi.org/10.1029/2010GL045896.

Frankenberg, C., Köhler, P., Magney, T.S., Geier, S., Lawson, P., Schwochert, M., McDuffie, J., Drewry, D.T., Pavlick, R., Kuhnert, A., 2018. The chlorophyll fluorescence imaging spectrometer (CFIS), mapping far red fluorescence from aircraft. Remote Sens. Environ. 217, 523–536. http://dx.doi.org/10.1016/j.rse.2018.08.032.

Gentine, P., Alemohammad, S.H., 2018. Reconstructed solar-induced fluorescence: A machine learning vegetation product based on MODIS surface reflectance to reproduce GOME-2 solar-induced fluorescence. Geophys. Res. Lett. 45 (7), 3136–3146. http://dx.doi.org/10.1002/2017GL076294.

Grace, J., Nichol, C., Disney, M., Lewis, P., Quaife, T., Bowyer, P., 2007. Can we measure terrestrial photosynthesis from space directly, using spectral reflectance and fluorescence? Global Change Biol. 13 (7), 1484–1497. http://dx.doi.org/10.1111/j.1365-2486.2007.01352.x.

Guanter, L., Aben, I., Tol, P., Krijger, J.M., Hollstein, A., Köhler, P., Damm, A., Joiner, J., Frankenberg, C., Landgraf, J., 2015a. Potential of the tropospheric monitoring instrument (TROPOMI) onboard the sentinel-5 precursor for the monitoring of terrestrial chlorophyll fluorescence. Atmos. Meas. Tech. http://dx.doi.org/10.5194/amt-8-1337-2015.

Guanter, L., Alonso, L., Gómez-Chova, L., Meroni, M., Preusker, R., Fischer, J., Moreno, J., 2010. Developments for vegetation fluorescence retrieval from spaceborne high-resolution spectrometry in the O2-A and O2-B absorption bands. J. Geophys. Res.: Atmos. 115 (D19), http://dx.doi.org/10.1029/2009JD013716.

Guanter, L., Bacour, C., Schneider, A., Aben, I., Van Kempen, T.A., Maignan, F., Retscher, C., Köhler, P., Frankenberg, C., Joiner, J., Zhang, Y., 2021. The TROPOSIF global sun-induced fluorescence dataset from the sentinel-5P TROPOMI mission. Earth Syst. Sci. Data 13 (11), 5423–5440. http://dx.doi.org/10.5194/essd-13-5423-2021.

Guanter, L., Frankenberg, C., Dudhia, A., Lewis, P.E., Gómez-Dans, J., Kuze, A., Suto, H., Grainger, R.G., 2012. Retrieval and global assessment of terrestrial chlorophyll fluorescence from GOSAT space measurements. Remote Sens. Environ. 121, 236–251. http://dx.doi.org/10.1016/j.rse.2012.02.006.

Guanter, L., Kaufmann, H., Segl, K., Foerster, S., Rogass, C., Chabrillat, S., Kuester, T., Hollstein, A., Rossner, G., Chlebek, C., Straif, C., Fischer, S., Schrader, S., Storch, T., Heiden, U., Mueller, A., Bachmann, M., Mühle, H., Müller, R., Habermeyer, M., Ohndorf, A., Hill, J., Buddenbaum, H., Hostert, P., Van der Linden, S., Leitão, P.J., Rabe, A., Doerffer, R., Krasemann, H., Xi, H., Mauser, W., Hank, T., Locherer, M., Rast, M., Staenz, K., Sang, B., 2015b. The EnMAP spaceborne imaging spectroscopy mission for earth observation. Remote Sens. 7 (7), 8830–8857. http://dx.doi.org/10.3390/rs70708830.

Guanter, L., Rossini, M., Colombo, R., Meroni, M., Frankenberg, C., Lee, J.-E., Joiner, J., 2013. Using field spectroscopy to assess the potential of statistical approaches for the retrieval of sun-induced chlorophyll fluorescence from ground and space. Remote Sens. Environ. 133, 52–61. http://dx.doi.org/10.1016/j.rse.2013.01.017.

Guanter, L., Zhang, Y., Jung, M., Joiner, J., Voigt, M., Berry, J.A., Frankenberg, C., Huete, A.R., Zarco-Tejada, P., Lee, J.-E., Moran, M.S., Ponce-Campos, G., Beer, C., Camps-Valls, G., Buchmann, N., Gianelle, D., Klumpp, K., Cescatti, A., Baker, J.M., Griffis, T.J., 2014. Global and time-resolved monitoring of crop photosynthesis with chlorophyll fluorescence. Proc. Natl. Acad. Sci. 111 (14), E1327–E1333. http://dx.doi.org/10.1073/pnas.1320008111.

Ioffe, S., Szegedy, C., 2015. Batch normalization: accelerating deep network training by reducing internal covariate shift. http://dx.doi.org/10.48550/arXiv.1502.03167, arXiv:1502.03167.

Joiner, J., Guanter, L., Lindstrot, R., Voigt, M., Vasilkov, A.P., Middleton, E.M., Huemmrich, K.F., Yoshida, Y., Frankenberg, C., 2013. Global monitoring of terrestrial chlorophyll fluorescence from moderate spectral resolution near-infrared satellite measurements: Methodology, simulations, and application to GOME-2. http://dx.doi.org/10.5194/amtd-6-3883-2013.

Joiner, J., Yoshida, Y., Guanter, L., Middleton, E.M., 2016. New methods for the retrieval of chlorophyll red fluorescence from hyperspectral satellite instruments: Simulations andapplication to GOME-2 and SCIAMACHY. Atmos. Meas. Tech. 9 (8), 3939–3967. http://dx.doi.org/10.5194/amt-9-3939-2016.

Joiner, J., Yoshida, Y., Vasilkov, A.P., Yoshida, Y., Corp, L.A., Middleton, E.M., 2011. First observations of global and seasonal terrestrial chlorophyll fluorescence from space. Biogeosciences 8 (3), 637–651. http://dx.doi.org/10.5194/bg-8-637-2011.

Jülich Supercomputing Centre, 2021. JURECA: data centric and booster modules implementing the modular supercomputing architecture at jülich supercomputing centre. J. Large-Scale Res. Facil. 7 (A182), http://dx.doi.org/10.17815/jlsrf-7-182.

Khanna, S., Liu, P., Zhou, L., Meng, C., Rombach, R., Burke, M., Lobell, D., Ermon, S., 2023. DiffusionSat: A generative foundation model for satellite imagery. arXiv:2312.03606.

Kim, J., Ryu, Y., Dechant, B., Lee, H., Kim, H.S., Kornfeld, A., Berry, J.A., 2021. Solar-induced chlorophyll fluorescence is non-linearly related to canopy photosynthesis in a temperate evergreen needleleaf forest during the fall transition. Remote Sens. Environ. 258, 112362. http://dx.doi.org/10.1016/j.rse.2021.112362.

Kingma, D.P., Ba, J., 2017. Adam: A method for stochastic optimization. http://dx.doi.org/10.48550/arXiv.1412.6980, arXiv:1412.6980.

Krämer, J., Siegmann, B., Kraska, T., Muller, O., Rascher, U., 2021. The potential of spatial aggregation to extract remotely sensed sun-induced fluorescence (SIF) of small-sized experimental plots for applications in crop phenotyping. Int. J. Appl. Earth Obs. Geoinf. 104, 102565. http://dx.doi.org/10.1016/j.jag.2021.102565.

Krutz, D., Müller, R., Knodt, U., Günther, B., Walter, I., Sebastian, I., Säuberlich, T., Reulke, R., Carmona, E., Eckardt, A., Venus, H., Fischer, C., Zender, B., Arloth, S., Lieder, M., Neidhardt, M., Grote, U., Schrandt, F., Gelmi, S., Wojtkowiak, A., 2019. The instrument design of the DLR earth sensing imaging spectrometer (DESIS). Sensors 19 (7), 1622. http://dx.doi.org/10.3390/s19071622.

Kurucz, R.L., 2006. High resolution irradiance spectrum from 300 to 1000 nm. http://dx.doi.org/10.48550/ARXIV.ASTRO-PH/0605029, URL https://arxiv.org/abs/astro-ph/0605029.

Lee, J.E., Berry, J.A., van der Tol, C., Yang, X., Guanter, L., Damm, A., Baker, I., Frankenberg, C., 2015. Simulations of chlorophyll fluorescence incorporated into the community land model version 4. Global Change Biol. http://dx.doi.org/10.1111/gcb.12948.

Liu, L., Liu, X., Wang, Z., Zhang, B., 2016. Measurement and analysis of bidirectional SIF emissions in wheat canopies. IEEE Trans. Geosci. Remote Sens. 54 (5), 2640–2651. http://dx.doi.org/10.1109/TGRS.2015.2504089.

Maes, W.H., Pagán, B.R., Martens, B., Gentine, P., Guanter, L., Steppe, K., Verhoest, N.E.C., Dorigo, W., Li, X., Xiao, J., Miralles, D.G., 2020. Sun-induced fluorescence closely linked to ecosystem transpiration as evidenced by satellite data and radiative transfer models. Remote Sens. Environ. 249, 112030. http://dx.doi.org/10.1016/j.rse.2020.112030.

Magney, T.S., Frankenberg, C., Köhler, P., North, G., Davis, T.S., Dold, C., Dutta, D., Fisher, J.B., Grossmann, K., Harrington, A., Hatfield, J., Stutz, J., Sun, Y., Porcar-Castell, A., 2019. Disentangling changes in the spectral shape of chlorophyll fluorescence: implications for remote sensing of photosynthesis. J. Geophys. Res.: Biogeosci. 124 (6), 1491–1507. http://dx.doi.org/10.1029/2019JG005029.

Maier, S.W., Günther, K.P., Stellmes, M., 2004. Sun-induced fluorescence: a new tool for precision farming. In: Digital Imaging and Spectral Techniques: Applications To Precision Agriculture and Crop Physiology. John Wiley & Sons, Ltd, pp. 207–222. http://dx.doi.org/10.2134/asaspecpub66.c16.

Mazzoni, M., Meroni, M., Fortunato, C., Colombo, R., Verhoef, W., 2012. Retrieval of maize canopy fluorescence and reflectance by spectral fitting in the O2–A absorption band. Remote Sens. Environ. 124, 72–82. http://dx.doi.org/10.1016/j.rse.2012.04.025.

Meroni, M., Busetto, L., Colombo, R., Guanter, L., Moreno, J., Verhoef, W., 2010. Performance of spectral fitting methods for vegetation fluorescence quantification. Remote Sens. Environ. 114 (2), 363–374. http://dx.doi.org/10.1016/j.rse.2009.09.010.

Mohammed, G.H., Colombo, R., Middleton, E.M., Rascher, U., van der Tol, C., Nedbal, L., Goulas, Y., Pérez-Priego, O., Damm, A., Meroni, M., Joiner, J., Cogliati, S., Verhoef, W., Malenovský, Z., Gastellu-Etchegorry, J.-P., Miller, J.R., Guanter, L., Moreno, J., Moya, I., Berry, J.A., Frankenberg, C., Zarco-Tejada, P.J., 2019. Remote sensing of solar-induced chlorophyll fluorescence (SIF) in vegetation: 50 years of progress. Remote Sens. Environ. 231, 111177. http://dx.doi.org/10.1016/j.rse.2019.04.030.

Naethe, P., De Sanctis, A., Burkart, A., Campbell, P.K., Colombo, R., Di Mauro, B., Damm, A., El-Madany, T., Fava, F., Gamon, J.A., Huemmrich, K.F., Migliavacca, M., Paul-Limoges, E., Rascher, U., Rossini, M., Schüttemeyer, D., Tagliabue, G., Zhang, Y., Julitta, T., 2024. Towards a standardized, ground-based network of hyperspectral measurements: Combining time series from autonomous field spectrometers with sentinel-2. Remote Sens. Environ. 303, 114013. http://dx.doi.org/10.1016/j.rse.2024.114013.

Naethe, P., Julitta, T., Chang, C.Y.-Y., Burkart, A., Migliavacca, M., Guanter, L., Rascher, U., 2022. A precise method unaffected by atmospheric reabsorption for ground-based retrieval of red and far-red sun-induced chlorophyll fluorescence. Agricult. Forest. Meterol. 325, 109152. http://dx.doi.org/10.1016/j.agrformet.2022.109152.

NASA JPL, 2013. NASA shuttle radar topography mission global 1 arc second. http://dx.doi.org/10.5067/MEASURES/SRTM/SRTMGL1.003.

Nordrhein-Westfalen, 2017. DTM 1m. Sonny's LiDAR digital terrain models of Europe, https://sonny.4lima.de/, Accessed: 2025/01/08.

Pato, M., Alonso, K., Auer, S., Buffat, J., Carmona, E., Maier, S., Müller, R., Rademske, P., Rascher, U., Scharr, H., 2023. Fast machine learning simulator of at-sensor radiances for solar-induced fluorescence retrieval with DESIS and hyplant. In: IGARSS 2023 - 2023 IEEE International Geoscience and Remote Sensing Symposium. pp. 7563–7566. http://dx.doi.org/10.1109/IGARSS52108.2023.10281579.

Pato, M., Buffat, J., Alonso, K., Auer, S., Carmona, E., Maier, S., Müller, R., Rademske, P., Rascher, U., Scharr, H., 2024. Physics-based machine learning emulator of At-sensor radiances for solar-induced fluorescence retrieval in the O_2-A absorption band. IEEE J. Sel. Top. Appl. Earth Obs. Remote Sens. 1–10. http://dx.doi.org/10.1109/JSTARS.2024.3457231.

Pierrat, Z., Magney, T., Parazoo, N.C., Grossmann, K., Bowling, D.R., Seibt, U., Johnson, B., Helgason, W., Barr, A., Bortnik, J., Norton, A., Maguire, A., Frankenberg, C., Stutz, J., 2022. Diurnal and seasonal dynamics of solar-induced chlorophyll fluorescence, vegetation indices, and gross primary productivity in the boreal forest. J. Geophys. Res.: Biogeosci. 127 (2), http://dx.doi.org/10.1029/2021JG006588, e2021JG006588.

Pignatti, S., Palombo, A., Pascucci, S., Romano, F., Santini, F., Simoniello, T., Umberto, A., Vincenzo, C., Acito, N., Diani, M., Matteoli, S., Corsini, G., Casa, R., De Bonis, R., Laneve, G., Ananasso, C., 2013. The PRISMA hyperspectral mission: science activities and opportunities for agriculture and land monitoring. In: 2013 IEEE International Geoscience and Remote Sensing Symposium - IGARSS. pp. 4558–4561. http://dx.doi.org/10.1109/IGARSS.2013.6723850.

Porcar-Castell, A., Tyystjärvi, E., Atherton, J., van der Tol, C., Flexas, J., Pfündel, E.E., Moreno, J., Frankenberg, C., Berry, J.A., 2014. Linking chlorophyll a fluorescence to photosynthesis for remote sensing applications: Mechanisms and challenges. J. Exp. Bot. 65 (15), 4065–4095. http://dx.doi.org/10.1093/jxb/eru191.

Rascher, U., Agati, G., Alonso, L., Cecchi, G., Champagne, S., Colombo, R., Damm, A., Daumard, F., de Miguel, E., Fernandez, G., Franch, B., Franke, J., Gerbig, C., Gioli, B., Gómez, J.A., Goulas, Y., Guanter, L., Gutiérrez-de-la-Cámara, Ó., Hamdi, K., Hostert, P., Jiménez, M., Kosvancova, M., Lognoli, D., Meroni, M., Miglietta, F., Moersch, A., Moreno, J., Moya, I., Neininger, B., Okujeni, A., Ounis, A., Palombi, L., Raimondi, V., Schickling, A., Sobrino, J.A., Stellmes, M., Toci, G., Toscano, P., Udelhoven, T., van der Linden, S., Zaldei, A., 2009. CEFLES2: The remote sensing component to quantify photosynthetic efficiency from the leaf to the region by measuring sun-induced fluorescence in the oxygen absorption bands. Biogeosciences 6 (7), 1181–1198. http://dx.doi.org/10.5194/bg-6-1181-2009.

Rascher, U., Baum, S., Siegmann, B., Buffat, J., Burkart, A., Cogliati, S., Colombo, R., Damm, A., Genesio, L., Hanus, J., Herrera, D., Julitta, T., Knopf, O., Miglietta, F., Muller, O., Quiros, J., 2022a. Flexsense: technical assistance for airborne measurements during the FLEX sentinel tandem experiment. http://dx.doi.org/10.57780/esa-84e5bf5.

Rascher, U., Siegmann, B., Baum, S., 2022b. Hyplant FLEX simulator on SAFIRE ATR42 for LIAISE experiment.

Rascher, U., Siegmann, B., Krieger, V., Matveeva, M., Quiros, J., Muller, O., Rademske, P., Herrera, D., Baum, S., Miglietta, F., Genesio, L., Colombo, R., Celesti, M., Tudoroiu, M., Cogliati, S., Carotenuto, F., Gioli, B., Genangelli, A., Hanus, J., Houlous, K., Migliavacca, M., Martini, D., Martin, M.P., Carrara, A., Moreno, G., Gonzales-Gascon, R., El-Madany, T., Pacheco-Labrador, J., Damm, A., Ahmed, R., Gupana, R., Paul-Limoges, E., Reiter, I., Xueref-Remy, I., Mevy, J.-P., Santonja, M., Bendig, J., Malenkovsky, Z., Julitta, T., Burkart, A., 2021. FLEX sentinel tandem campaign: technical assistance for airborne measurements during the FLEX sentinel tandem experiment. http://dx.doi.org/10.57780/esa-ae7953d.

Rossini, M., Nedbal, L., Guanter, L., Ač, A., Alonso, L., Burkart, A., Cogliati, S., Colombo, R., Damm, A., Drusch, M., Hanus, J., Janoutova, R., Julitta, T., Kokkalis, P., Moreno, J., Novotny, J., Panigada, C., Pinto, F., Schickling, A., Schüttemeyer, D., Zemek, F., Rascher, U., 2015. Red and far red sun-induced chlorophyll fluorescence as a measure of plant photosynthesis. Geophys. Res. Lett. 42 (6), 1632–1639. http://dx.doi.org/10.1002/2014GL062943.

Ryu, Y., Berry, J.A., Baldocchi, D.D., 2019. What is global photosynthesis? history, uncertainties and opportunities. Remote Sens. Environ. 223, 95–114. http://dx.doi.org/10.1016/j.rse.2019.01.016.

Sabater, N., Kolmonen, P., Van Wittenberghe, S., Arola, A., Moreno, J., 2021. Challenges in the atmospheric characterization for the retrieval of spectrally resolved fluorescence and PRI region dynamics from space. Remote Sens. Environ. 254, 112226. http://dx.doi.org/10.1016/j.rse.2020.112226.

Siegmann, B., Alonso, L., Celesti, M., Cogliati, S., Colombo, R., Damm, A., Douglas, S., Guanter, L., Hanuš, J., Kataja, K., Kraska, T., Matveeva, M., Moreno, J., Muller, O., Pikl, M., Pinto, F., Quirós Vargas, J., Rademske, P., Rodriguez-Morene, F., Sabater, N., Schickling, A., Schüttemeyer, D., Zemek, F., Rascher, U., 2019. The high-performance airborne imaging spectrometer hyplant—from raw images to top-of-canopy reflectance and fluorescence products: introduction of an automatized processing chain. Remote Sens. 11 (23), 2760. http://dx.doi.org/10.3390/rs11232760.

Siegmann, B., Cendrero-Mateo, M.P., Cogliati, S., Damm, A., Gamon, J., Herrera, D., Jedmowski, C., Junker-Frohn, L.V., Kraska, T., Muller, O., Rademske, P., van der Tol, C., Quiros-Vargas, J., Yang, P., Rascher, U., 2021. Downscaling of far-red solar-induced chlorophyll fluorescence of different crops from canopy to leaf level using a diurnal data set acquired by the airborne imaging spectrometer hyplant. Remote Sens. Environ. 264, 112609. http://dx.doi.org/10.1016/j.rse.2021.112609.

Subhash, N., Mohanan, C.N., 1997. Curve-fit analysis of chlorophyll fluorescence spectra: application to nutrient stress detection in sunflower. Remote Sens. Environ. 60 (3), 347–356. http://dx.doi.org/10.1016/S0034-4257(96)00217-9.

Sun, Y., Frankenberg, C., Jung, M., Joiner, J., Guanter, L., Köhler, P., Magney, T., 2018. Overview of solar-induced chlorophyll fluorescence (SIF) from the orbiting carbon observatory-2: retrieval, cross-mission comparison, and global monitoring for GPP. Remote Sens. Environ. http://dx.doi.org/10.1016/j.rse.2018.02.016.

Sun, Y., Frankenberg, C., Wood, J.D., Schimel, D.S., Jung, M., Guanter, L., Drewry, D.T., Verma, M., Porcar-Castell, A., Griffis, T.J., Gu, L., Magney, T.S., Köhler, P., Evans, B., Yuen, K., 2017. OCO-2 advances photosynthesis observation from space via solar-induced chlorophyll fluorescence. Science http://dx.doi.org/10.1126/science.aam5747.

Tagliabue, G., Panigada, C., Dechant, B., Baret, F., Cogliati, S., Colombo, R., Migliavacca, M., Rademske, P., Schickling, A., Schüttemeyer, D., Verrelst, J., Rascher, U., Ryu, Y., Rossini, M., 2019. Exploring the spatial relationship between airborne-derived red and far-red sun-induced fluorescence and process-based GPP estimates in a forest ecosystem. Remote Sens. Environ. 231, 111272. http://dx.doi.org/10.1016/j.rse.2019.111272.

Tarquini, S., Isola, I., Favalli, M., Battistini, A., Dotta, G., 2023. TINITALY, a digital elevation model of Italy with a 10 meters cell size (version 1.1). http://dx.doi.org/10.13127/TINITALY/1.1.

Thompson, D.R., Bohn, N., Brodrick, P.G., Carmon, N., Eastwood, M.L., Eckert, R., Fichot, C.G., Harringmeyer, J.P., Nguyen, H.M., Simard, M., Thorpe, A.K., 2022. Atmospheric lengthscales for global VSWIR imaging spectroscopy. J. Geophys. Res.: Biogeosci. 127 (6), http://dx.doi.org/10.1029/2021JG006711, e2021JG006711.

Thompson, D.R., Kahn, B.H., Brodrick, P.G., Lebsock, M.D., Richardson, M., Green, R.O., 2021. Spectroscopic imaging of sub-kilometer spatial structure in lower-tropospheric water vapor. Atmos. Meas. Tech. 14 (4), 2827–2840. http://dx.doi.org/10.5194/amt-14-2827-2021.

van der Tol, C., Berry, J.A., Campbell, P.K.E., Rascher, U., 2014. Models of fluorescence and photosynthesis for interpreting measurements of solar-induced chlorophyll fluorescence. J. Geophys. Res.: Biogeosci. 119 (12), 2312–2327. http://dx.doi.org/10.1002/2014JG002713.

van der Tol, C., Julitta, T., Yang, P., Sabater, N., Reiter, I., Tudoroiu, M., Schuettemeyer, D., Drusch, M., 2023. Retrieval of chlorophyll fluorescence from a large distance using oxygen absorption bands. Remote Sens. Environ. 284, 113304. http://dx.doi.org/10.1016/j.rse.2022.113304.

van der Tol, C., Rossini, M., Cogliati, S., Verhoef, W., Colombo, R., Rascher, U., Mohammed, G., 2016. A model and measurement comparison of diurnal cycles of sun-induced chlorophyll fluorescence of crops. Remote Sens. Environ. 186, 663–677. http://dx.doi.org/10.1016/j.rse.2016.09.021.

van der Tol, C., Verhoef, W., Timmermans, J., Verhoef, A., Su, Z., 2009. An integrated model of soil-canopy spectral radiances, photosynthesis, fluorescence, temperature and energy balance. Biogeosciences 6 (12), 3109–3129. http://dx.doi.org/10.5194/bg-6-3109-2009.

Verrelst, J., De Grave, C., Amin, E., Reyes, P., Morata, M., Portales, E., Belda, S., Tagliabue, G., Panigada, C., Boschetti, M., Candiani, G., Segl, K., Guillasso, S., Berger, K., Wocher, M., Hank, T., Rascher, U., Isola, C., 2021. Prototyping vegetation traits models in the context of the hyperspectral chime mission preparation. In: 2021 IEEE International Geoscience and Remote Sensing Symposium IGARSS. pp. 7678–7681. http://dx.doi.org/10.1109/IGARSS47720.2021.9554407.

Verrelst, J., Rivera, J.P., van der Tol, C., Magnani, F., Mohammed, G., Moreno, J., 2015. Global sensitivity analysis of the SCOPE model: what drives simulated canopy-leaving sun-induced fluorescence? Remote Sens. Environ. 166, 8–21. http://dx.doi.org/10.1016/j.rse.2015.06.002.

Verrelst, J., Rivera Caicedo, J.P., Muñoz-Marí, J., Camps-Valls, G., Moreno, J., 2017. SCOPE-based emulators for fast generation of synthetic canopy reflectance and sun-induced fluorescence spectra. Remote Sens. 9 (9), 927. http://dx.doi.org/10.3390/rs9090927.

Verrelst, J., Sabater, N., Rivera, J.P., Muñoz-Marí, J., Vicent, J., Camps-Valls, G., Moreno, J., 2016. Emulation of leaf, canopy and atmosphere radiative transfer models for fast global sensitivity analysis. Remote Sens. 8 (8), 673. http://dx.doi.org/10.3390/rs8080673.

Vicent, J., Sabater, N., Tenjo, C., Acarreta, J.R., Manzano, M., Rivera, J.P., Jurado, P., Franco, R., Alonso, L., Verrelst, J., Moreno, J., 2016. FLEX end-to-end mission performance simulator. IEEE Trans. Geosci. Remote Sens. 54 (7), 4215–4223. http://dx.doi.org/10.1109/TGRS.2016.2538300.

Vicent, J., Verrelst, J., Rivera-Caicedo, J.P., Sabater, N., Muñoz-Marí, J., Camps-Valls, G., Moreno, J., 2018. Emulation as an accurate alternative to interpolation in sampling radiative transfer codes. IEEE J. Sel. Top. Appl. Earth Obs. Remote Sens. 11 (12), 4918–4931. http://dx.doi.org/10.1109/JSTARS.2018.2875330.

Wang, N., Siegmann, B., Rascher, U., Clevers, J.G.P.W., Muller, O., Bartholomeus, H., Bendig, J., Masiliūnas, D., Pude, R., Kooistra, L., 2022. Comparison of a UAV- and an airborne-based system to acquire far-red sun-induced chlorophyll fluorescence measurements over structurally different crops. Agricult. Forest. Meterol. 323, 109081. http://dx.doi.org/10.1016/j.agrformet.2022.109081.

Wang, N., Suomalainen, J., Bartholomeus, H., Kooistra, L., Masiliūnas, D., Clevers, J.G.P.W., 2021. Diurnal variation of sun-induced chlorophyll fluorescence of agricultural crops observed from a point-based spectrometer on a UAV. Int. J. Appl. Earth Obs. Geoinf. 96, 102276. http://dx.doi.org/10.1016/j.jag.2020.102276.

Wang, D., Zhang, Q., Xu, Y., Zhang, J., Du, B., Tao, D., Zhang, L., 2023. Advancing plain vision transformer toward remote sensing foundation model. IEEE Trans. Geosci. Remote Sens. 61, 1–15. http://dx.doi.org/10.1109/TGRS.2022.3222818.

Wieneke, S., Ahrends, H., Damm, A., Pinto, F., Stadler, A., Rossini, M., Rascher, U., 2016. Airborne based spectroscopy of red and far-red sun-induced chlorophyll fluorescence: Implications for improved estimates of gross primary productivity. Remote Sens. Environ. 184, 654–667. http://dx.doi.org/10.1016/j.rse.2016.07.025.

Wu, Y., He, K., 2018. Group normalization. (arXiv:1803.08494), http://dx.doi.org/10.48550/arXiv.1803.08494.

Yao, L., Yang, D., Liu, Y., Wang, J., Liu, L., Du, S., Cai, Z., Lu, N., Lyu, D., Wang, M., Yin, Z., Zheng, Y., 2021. A new global solar-induced chlorophyll fluorescence (SIF) data product from TanSat measurements. Adv. Atmos. Sci. 38 (3), 341–345. http://dx.doi.org/10.1007/s00376-020-0204-6.

Zarco-Tejada, P., González-Dugo, M., Fereres, E., 2016. Seasonal stability of chlorophyll fluorescence quantified from airborne hyperspectral imagery as an indicator of net photosynthesis in the context of precision agriculture. Remote Sens. Environ. 179, 89–103. http://dx.doi.org/10.1016/j.rse.2016.03.024.

Zhang, Y., Joiner, J., Alemohammad, S.H., Zhou, S., Gentine, P., 2018. A global spatially contiguous solar-induced fluorescence (CSIF) dataset using neural networks. Biogeosciences 15 (19), 5779–5800. http://dx.doi.org/10.5194/bg-15-5779-2018.